Biophysical Journal Volume 108 May 2015 2258–2269

Article

Coarse-Grained Model of SNARE-Mediated Docking

Nicole Fortoul,[1] Pankaj Singh,[3] Chung-Yuen Hui,[3] Maria Bykhovskaia,[4] and Anand Jagota[1,2,*]
[1]Department of Chemical and Biomolecular Engineering and [2]Bioengineering Program, Lehigh University, Bethlehem, Pennsylvania; [3]Department of Mechanical & Aerospace Engineering, Cornell University, Ithaca, New York; and [4]Neuroscience Department, Universidad Central del Caribe, Bayamon, Puerto Rico

ABSTRACT Synaptic transmission requires that vesicles filled with neurotransmitter molecules be docked to the plasma membrane by the SNARE protein complex. The SNARE complex applies attractive forces to overcome the long-range repulsion between the vesicle and membrane. To understand how the balance between the attractive and repulsive forces defines the equilibrium docked state we have developed a model that combines the mechanics of vesicle/membrane deformation with an apparently new coarse-grained model of the SNARE complex. The coarse-grained model of the SNARE complex is calibrated by comparison with all-atom molecular dynamics simulations as well as by force measurements in laser tweezer experiments. The model for vesicle/membrane interactions includes the forces produced by membrane deformation and hydration or electrostatic repulsion. Combining these two parts, the coarse-grained model of the SNARE complex with membrane mechanics, we study how the equilibrium docked state varies with the number of SNARE complexes. We find that a single SNARE complex is able to bring a typical synaptic vesicle to within a distance of ~3 nm from the membrane. Further addition of SNARE complexes shortens this distance, but an overdocked state of >4–6 SNAREs actually increases the equilibrium distance.

INTRODUCTION

The soluble *n*-ethylmaleimide-sensitive-factor attachment protein receptor (SNARE) (1,2) complexes are the core protein machinery involved in synaptic vesicle docking and fusion. SNARE proteins form a link between vesicles and the plasma membrane, providing a mechanism for zippering the two together. The transmembrane vesicle-associated protein synaptobrevin (Syb or v-SNARE) forms a four-helix bundle with the proteins SNAP-25 and the transmembrane protein syntaxin (Syx), which are attached to the neuronal plasma membrane and termed the "t-SNARE". SNAP-25 contributes two helices (SN1 and SN2) to the bundle, while both Syx and Syb contribute one helix each (3,4). During exocytosis the vesicles are first tethered or targeted toward the plasma membrane (>25 nm (5)), then they are docked at the plasma membrane with the help of the adhesive forces provided by SNAREs. After docking, priming occurs, which finally leads to vesicle-to-membrane fusion (1). The zippering of the SNARE bundle is thought to provide the necessary force to bring the vesicle in proximity to the plasma membrane by overcoming the hydration or electrostatic repulsion between the two.

The process of synaptic vesicle docking and fusion can be viewed as deformation of a mechanical system, in which a synaptic vesicle, a nearly spherical lipid bilayer shell, is brought in proximity to the plasma membrane, a nearly flat lipid bilayer, under the influence of the attractive forces exerted by the SNARE complex. Key structural characteristics of the SNARE bundle have been determined experimentally, including its x-ray crystal structure (6) and the location of the layers thought to be essential to SNARE's function (7), which have been confirmed through single molecule force experiments (8). All-atom simulations have been performed to analyze the structural aspects of the SNARE bundle including detailed interactions between the different helices (9) as well as to investigate the effects of oxidation and reduction of the SNAP25 linker domain on the formation of the SNARE bundle (10). Some all-atom simulation work has been done on the unzippering of the SNARE bundle (11), but time constraints prevent simulations for large displacements and longer timescales. In an effort to overcome timescale limitations, some coarse-grained (CG) simulations have been performed (12,13). Force fields for CG simulations have been developed (14). However, to suit a wide range of applications, these force fields still need to be refined (15). Relatively little has been done on coupling the SNARE unzipping process to the vesicle-plasma membrane behavior to address questions including that of how docking depends on the number of SNAREs. This problem is difficult because it must capture large length-scale deformations and electrostatics in the vesicle-plasma membrane system as well as the amino-acid-level chemical specificity essential to the functioning of the SNARE bundle.

There is significant debate about how many SNARE complexes are required to make synaptic fusion happen. Earlier studies suggested that 5–8 SNARE complexes form the fusion pore (16). However, recent studies suggest a smaller number of SNARE complexes. Thus, it was suggested

Submitted October 15, 2014, and accepted for publication March 24, 2015.
*Correspondence: anj6@lehigh.edu
Editor: Tobias Baumgart.

0006-3495/15/05/2258/12 $2.00
http://dx.doi.org/10.1016/j.bpj.2015.03.053

recently that a single SNARE complex can trigger fusion (17), while stating the fact that the fusion rate increases with the number of SNAREs. In Sinha et al. (18), it has been proposed that two Syb units are required for fusion, based on fluorescence response of tagged Syb. The work done in Mohrmann et al. (19) suggests that three SNARE units are needed to carry out the fusion, on the basis of fusion rate. At the same time, studies performed on model systems in vitro suggest numbers ranging between 5 and 11 (20).

To investigate how the number of SNARE complexes affects vesicle docking, we developed a continuum model of the lipid bilayers and combined it with a CG model for the SNARE that includes chemical specificity. Specifically, the proteins in the SNARE bundle are represented by an α-carbon-based CG model that includes both structural and chemical specificity by employing an elastic network model (ENM) (21,22) and Miyazawa and Jernigan (23–25) contact energies, respectively. The SNARE CG model is calibrated to match the peak unzipping force determined by Gao et al. (8), and is used to calculate a force displacement curve for the unzipping process, along with snapshots of corresponding structures that provide information about the unzipping pathway. The continuum model for bilayer deformation is based on lipid membrane theory developed in Jenkins et al. (26) and is an extension of work done in Long et al. (27). It computes the force required to counter the vesicle-membrane repulsion, bringing the vesicle to a given distance from the membrane while taking full account of the vesicle and membrane deformation. Balancing the SNARE-induced attraction against the vesicle-membrane hydration or electrostatic repulsion provides us with information on the equilibrium gap between the two membranes for a given number of SNAREs. Based on this information, we study the effect of the number of SNAREs from the point of view of the mechanics of the process.

MATERIALS AND METHODS

All-atom simulations

We conducted all-atom molecular simulations of SNARE helices in order to obtain some of the parameters for the SNARE CG model. All-atom (AA) simulations of the four individual helices as well as the full SNARE bundle were performed using the GROMACS molecular simulation package (28) and the CHARM22 force field (29). The starting structures for the four individual helices and the full SNARE bundle were extracted from the final timestep of a 40-ns AA simulation with initial configuration given by the high-resolution x-ray structure PDB:1N7S (7,11). (See the Supporting Material for a discussion.) For each set of runs, the corresponding structure was solvated in a waterbox ($70 \times 150 \times 70$ Å), and potassium ions were added to neutralize the overall charge. Additional potassium and chloride ions were added so that there was a 150-mM concentration of KCl to mimic physiological conditions (30). All bonds were constrained. Dynamics were run at 300 K first using an NVT ensemble for 100 ps followed by NPT for 100 ps using the Parrinello-Rahman barostat. Five sets of 40-ns-long runs were conducted with a timestep of 2 fs for Syb, Syx, SN1, SN2, and the SNARE bundle. Computations were performed at the Texas Advanced Computing Center (Austin, TX) through Extreme Science and Engineering Discovery Environment (XSEDE) resources.

SNARE coarse-grained model

A principal result of this work is the development of a CG model for the SNARE complex. Our goal has been to make it as simple as possible while retaining the identity of individual residues. As shown in Fig. 1 *A*, in our SNARE model every residue is represented by a bead located at the α-carbon of that residue.

The size and mass of each bead are equivalent to the van der Waals radius and mass (31) of the bead's corresponding residue. Two major types of interactions were accounted for in this CG model—those within individual helices, and those between them. An ENM (21,22) is used to represent the intrahelical bonds and interactions that maintain the individual helical structure as shown in Fig. 1 *A*. Pairs of beads within the cutoff distance, R_c, on the same helix are said to be in contact and are connected by a harmonic spring with the energy potential

$$u_{\text{spring}} = \frac{1}{2}k_s(r - r_0)^2, \tag{1}$$

where k_s is the spring constant, r is the distance between the two beads, and r_0 is the natural length of the spring. From the 40-ns-long individual helix AA simulations, it was observed that the natural state of each individual helix was a relatively straight conformation compared to the helices in the SNARE x-ray crystal structure. (The mean curvature of the helices in the SNARE bundle (3.11×10^7 l/m) is three times as large as that of the individual helices (1.03×10^7 l/m; see the Supporting Material.)) Because these straightened-out conformations represent the natural or relaxed state of the helices, they were used to construct the ENM. This is important because, as the helices unzip from the main bundle and break their helix-helix contacts, they revert to their natural straight conformation, releasing elastic energy.

The values of k_s for the ENM were chosen by matching the spectrum of fluctuations of the AA simulations and the CG model for each helix independently. For the analysis of individual AA helix simulations, the positions of the α-carbons were extracted every 10 ps. For each α-carbon a time series of distance from its average location was calculated. The fast Fourier transform was then computed for each bead's time series and averaged over all beads, yielding a single spectrum per helix. In order to make this comparison of the fluctuations, CG simulations were conducted for the four individual helices using Langevin dynamics at 300 K for a range of values of k_s. (Details on numerical implementation of the CG simulation are provided in the Supporting Material.) The same fast Fourier transform analysis was conducted for individual helix CG simulations as the AA simulations. The time length of simulations required was determined by conducting a normal modes analysis on the CG model of the crystal structure, PDB:1N7S, for all helices individually using different values of k_s. AA simulations were run for 2 ns, which is considerably longer than the characteristic time given as the inverse of the lowest natural frequency (see Table S1 in the Supporting Material). In order to best match the fluctuations, the root-mean-squared deviation between the AA and CG spectra was found for each run. An example of the comparison of both spectra is shown in Fig. 1 *B* for Syb with k_s value of 0.0963 N/m. For all helices, k_s was varied between 0.00009 N/m and 0.4816 N/m and the resulting root-mean-squared deviations for all values of k_s are shown in the Supporting Material. Based on these data, a value of 0.0963 N/m was chosen for k_s for all four helices.

The second main category of interaction in the CG model is the helix-helix interaction, which requires chemical specificity. These interactions are implemented by utilizing the contact energies from Miyazawa and Jernigan (23–25), which provide a scalable reference for residue-residue interactions (23–25). Any beads on separate helices interact if they are within the Miyazawa and Jernigan (23–25) cutoff distance, R_{c_MJ}. To avoid checking

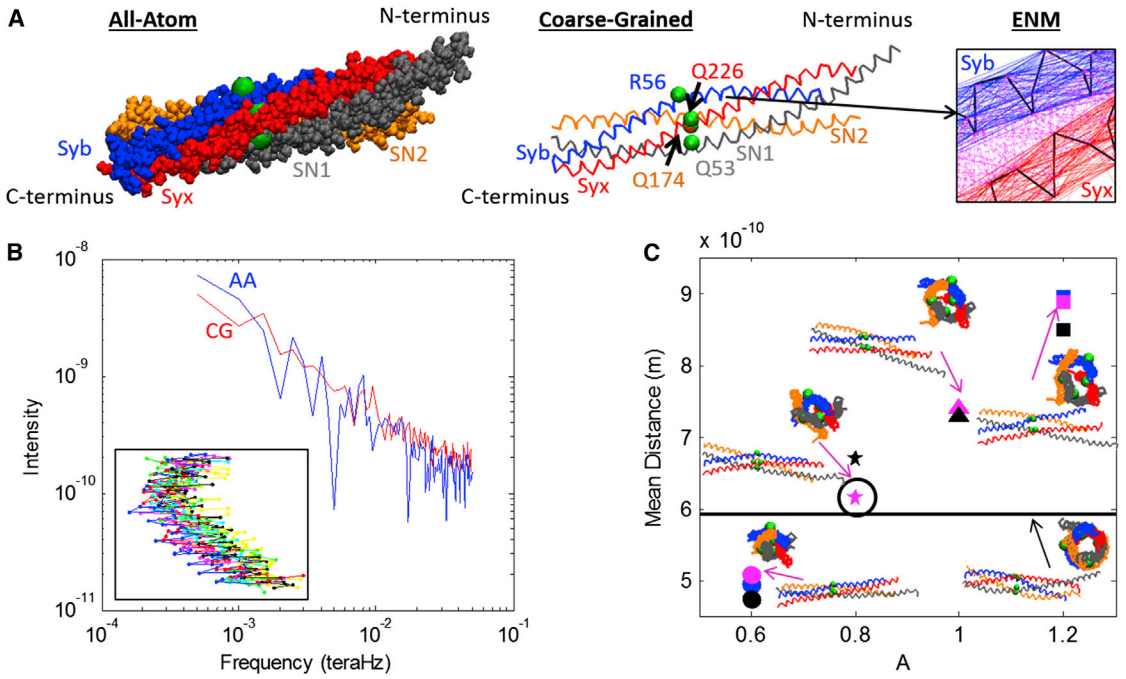

FIGURE 1 (*A*) The AA (*left*) and CG (*middle*) representations of the SNARE bundle are shown. Both models include helices Syb, Syx, SN1, and SN2 with each helix contributing one residue to the ionic layer (*beads*): R56, Q226, Q53, and Q174 respectively. The C-terminal ends of Syb and Syx play an integral role in the fusion process in that they attach to the vesicle (Syb) and plasma membrane (Syx). The ENM spring network (*right*) that maintains the individual helical structure is shown for Syb and Syx. (*Thick lines*) C_α backbones; (*thin lines*) ENM springs. The Miyazawa and Jernigan (23–25) contacts between Syb and Syx are also represented (*dotted lines*). (*B*) The spectra used to compare the fluctuations of the AA and CG models are shown for Syb. Values for k_s of 0.0963 N/m and R_c of 20 Å were used for the CG model. (*Inset*) Ten snapshots of Syb during the corresponding AA simulation. (*C*) Mean distance for different values of parameter *A* along with snapshots of the SNARE bundle. (*Black line*) Original crystal. (*Black circle*) Version chosen for simulation. To see this figure in color, go online.

the distance between every bead during every timestep, a neighbor list is built every 1000 steps. Any beads on different helices that are within $1.5*R_{c\_MJ}$ of each other are added to the neighbor list. Contacts are determined from the pairs already chosen by the neighbor list.

Following Kim and Hummer (32), the interaction energy ε_{ij} between residues i and j of the SNARE structure is scaled from the Miyazawa and Jernigan (23–25) contact energies e_{ij} (32):

$$\varepsilon_{ij} = \lambda\left(e_{ij} - e_0\right). \tag{2}$$

Note that there is no self-interaction, i.e., Eq. 2 applies only for $i \neq j$. Also, these interactions operate only between residues on different helices, intra-helical interactions being already represented by the ENM. There are two tunable parameters—a scaling parameter, λ, and a shifting parameter, e_0. Throughout the tuning of parameters, e_0 was set to 0. Although it was available as an extra parameter, it was not found necessary to match the SNARE structure and hence was not used in order to minimize the number of adjustable parameters.

Forces corresponding to the contact energies from Miyazawa and Jernigan (23–25) are implemented using a slightly modified 6-12 LJ potential. The format of this potential varies depending on whether there is attraction or repulsion between these residues as well as if the distance between beads is greater than or less than that the distance at which the potential minimum occurs, r_{ij}^0. The sign of ε_{ij} determines whether the interaction between the residues is attractive (negative) or repulsive (positive). The modified Lennard-Jones potentials (32) are as follows:

if $\varepsilon_{ij} < 0$,

$$u_{ij}(r) = 4\left|\varepsilon_{ij}\right|\left[\left(\frac{\sigma_{ij}}{r}\right)^{12} - \left(\frac{\sigma_{ij}}{r}\right)^{6}\right]; \tag{3}$$

if $\varepsilon_{ij} > 0$ and $r < r_{ij}^0$,

$$u_{ij}(r) = 4\left|\varepsilon_{ij}\right|\left[\left(\frac{\sigma_{ij}}{r}\right)^{12} - \left(\frac{\sigma_{ij}}{r}\right)^{6}\right] + 2\varepsilon_{ij}; \tag{4}$$

and if $\varepsilon_{ij} > 0$ and $r \geq r_{ij}^0$,

$$u_{ij}(r) = -4\left|\varepsilon_{ij}\right|\left[\left(\frac{\sigma_{ij}}{r}\right)^{12} - \left(\frac{\sigma_{ij}}{r}\right)^{6}\right], \tag{5}$$

where r is the distance between the two beads and σ_{ij} is the interaction radii. Eq. 4 contains a shift in the potential that ensures that repulsive pairs of beads will always repel each other.

The interaction radii is defined as the average of the van der Waals radii of residues i and j,

$$\sigma_{ij} = A * \frac{\sigma_i + \sigma_j}{2}, \tag{6}$$

where A is available as a tuning parameter and σ_i and σ_j are the van der Waals radii of residues i and j. In order to match both CG and AA behavior and structure, A was adjusted to match the SNARE bundle width, defined as the diameter of the tube-shaped space inside the bundle that can be seen if one looks along the center axis of SNARE. The reference bundle width was found by computing the mean distance of all of the nearest contacts of Miyazawa and Jernigan (23–25) from the SNARE crystal structure determined from PDB:1N7S. These 21 nearest contacts represent the distances between the inner residues of the bundle and therefore the bundle width. Fig. 1 *C* shows the mean distance for a few cases. The value of A is directly

related to bundle width, and from Fig. 1 *C* we chose a value of A as 0.8 to produce a similar mean bundle width to the crystal structure. This value of A corresponds to interaction radii ranging from 3.6 Å for Gly-Gly and 5.44 Å for Trp-Trp (32).

The remaining parameter, λ, controls the strength of interhelical interactions and was determined by calibrating the results of simulated force-extension behavior of the SNARE complex by the recent experimental study by Gao et al. (8), which provided characteristic forces for the unzipping of the 4-helix SNARE bundle pulled apart in an optical tweezer experiment. The value of λ was calibrated to match the measured peak force of 14–19 pN (specifically, 17.2 pN). For our unzipping simulation, the C-terminal residues of Syx and Syb were each attached to a fixed bead by a spring with a spring constant k_{spb}. Displacement control was used on the bead attached to the C-terminal Syb bead as opposed to the actual Syb C-terminal bead, to allow for rotation of the SNARE bundle.

To see how much the orientation of the pulling force on the SNARE matters, the simulations were performed in two ways: by applying a displacement to pulling beads attached to Syb89 and Syx256 through a spring (as shown in the article); and by directly applying displacements to Syb89 and Syx256. (The pulling beads allow for rotation of the SNARE bundle during the simulation and are hence less restrictive.) The results of these simulations were quite similar. To mimic the experimental setup in which the N-termini of Syx and Syb are connected, a FENE bond connecting the N-terminal residues of Syb and Syx was incorporated in the model to represent the additional residues, and the N-terminal disulfide bridge from the experiment of Gao et al. (8) is included. The potentials used to implement the FENE bond are as follows:

if $r(t) < r_{c\_FENE}$,

$$u_{FENE}(t) = -\frac{1}{2}k_F r_0^2 \ln\left(1 - \left(\frac{r(t)-\Delta}{r_0}\right)^2\right); \quad (7)$$

and if $r(t) \geq r_{c\_FENE}$,

$$u_{FENE}(t) = -\frac{1}{2}k_F (r(t)-\Delta)^2, \quad (8)$$

where r is the distance between two bonds at t; r_0 is the maximum bond length; Δ is the resting bond length or, in this case, the original distance between the two beads (33); and r_{c_FENE} is 0.9*Δ. The value of r_0 was determined by the number of residues that the spring represents, eight for Syb and five for Syx, times the maximum extension per residue, 3.65 Å (8). The FENE spring constant, k_F, used was the same as k_s for the ENM of 0.0963 N/m.

Before beginning the CG displacement control simulations, the SNARE structure was relaxed for 10^6 timesteps under quasi-static conditions, i.e., at 0 Kelvin. This relaxation was performed on the SNARE structure extracted from the final timestep of the 40 ns AA simulation in order to ensure that the initial structure was fully equilibrated. After this relaxation period, the C-termini beads were separated under displacement control using the two pulling beads that were discussed previously. The bead attached to the Syx C-terminus was held fixed, and all displacements were applied to the bead attached to the C-terminal Syb bead. For each displacement, this bead was moved 1 Å along the vector between the two pulling beads. After each displacement was applied, the structure was relaxed for 10^5 timesteps in order to allow it to equilibrate. At the end of the relaxation period, the forces on both pulling beads were nearly identical, and these forces were recorded as a function of displacement (see Fig. S4 in the Supporting Material).

Displacement control runs were conducted with 11 different values of λ between 0.16 and 0.72. This parameter directly adjusted the magnitude of the force, so it was used to match the peak unzipping force reported by Gao et al. (8) of between 14 and 19 pN. On this basis, a value of 0.3 was chosen to produce a peak force in the experimentally measured range of 17.2 pN.

Continuum model of the vesicle and plasma membrane

The vesicle and plasma membrane are subjected to forces from the SNARE complex drawing them together, and distributed distance-dependent electrostatic and hydration repulsion. During this process, the vesicle and plasma membrane both deform considerably and the task of the continuum model is to obtain a consistent solution of the deformed shape subject to these forces. The continuum calculations are based on the formulation of Jenkins et al. (26) and its extension to SNARE-mediated fusion by Long et al. (27). Our axisymmetric continuum model extends these formulations to include concentrated forces due to the SNARE molecules and the electrostatic forces due to the charges on the membranes or hydration repulsion.

The axisymmetric geometry is shown schematically in Fig. 2. We use a cylindrical coordinate system (r,θ,z), where θ is the angle of revolution about the z axis. Owing to the axisymmetric assumption, the forces exerted by the zipping of the SNARE complexes are represented by a circle of line force of magnitude F on a spherical vesicle of radius R (see Fig. 2 *B*) as well as on the plasma membrane. This line force counters the repulsive forces between the vesicle and the plasma membrane. As shown in Fig. 2 *B*, the line force acts along a latitude of the undeformed vesicle and is constrained to remain normal to the deformed surface. The location of the latitude is specified by the arc length S_0 of a cross section in the reference configuration, which is taken to be a spherical vesicle. Because the plasma membrane is very large compared to the vesicle radius, its reference configuration is taken to be a flat circular membrane of radius L under pre-tension, T_0. The SNARE forces act on a circle of radius S_0 in the reference configuration, have the same magnitude F, and are always directed opposite to the force on the vesicle (Fig. 2, *B* and *C*).

In our model, the repulsive force depends only on the local separation δ, as shown schematically in Fig. 2. Following Bykhovskaia et al. (11), electrostatic and hydration repulsion between the vesicle and plasma membrane are calculated using Derjaguin's approximation (34) in which interaction between curved surfaces is estimated assuming that the surfaces are locally flat. This approximation is valid if the length scale over which forces decay is much smaller than the radius of curvature of the vesicle. The applicable range of separations before vesicle to membrane fusion is 2–4 nm. In this range, the principal repulsive forces are due to electrostatics and hydration.

The functional form of both the electrostatic and hydration repulsion is approximately the same, an exponential decay. Electrostatics has the large decay length (typically 1 nm under physiological conditions) and smaller prefactor (34). The decay length for hydration repulsion is in the 1–4 Å range (34–37). Consequently, hydration dominates for small separation and electrostatics for larger separation. Much of the previous work suggests that the cross-over distance beyond which electrostatics dominates is ~1.5 nm (34,36). However, recent work of Aeffner et al. (35) suggests that hydration repulsion exceeds electrostatic repulsion for distances up to ~3 nm. Based on the work of Aeffner et al. (35), we have performed calculations taking hydration repulsion to be the dominant repulsive interaction. However, given some uncertainty regarding the relative importance of electrostatics and hydration, we have also computed results for the case where electrostatic repulsion is assumed to dominate. The hydration pressure takes on the form of an exponential decay,

$$P(d_w) = P_0 \exp(-d_w/\lambda_h), \quad (9)$$

where d_w is the lipid bilayer separation, P_0 is the hydration pressure amplitude, and λ_h is the decay length. According to Aeffner et al. (35), the prefactor, P_0, ranges from 0.24 to 4.13 GPa and λ_h ranges from 2.3 to 3.7 Å. We chose to use a value of 0.43 GPa for P_0 and a λ_h of 3.22 Å based on the parameters suggested for a synaptic vesicle corresponding to experiments performed in a physiologically relevant DOPC/Chol 70:30 mixture (35).

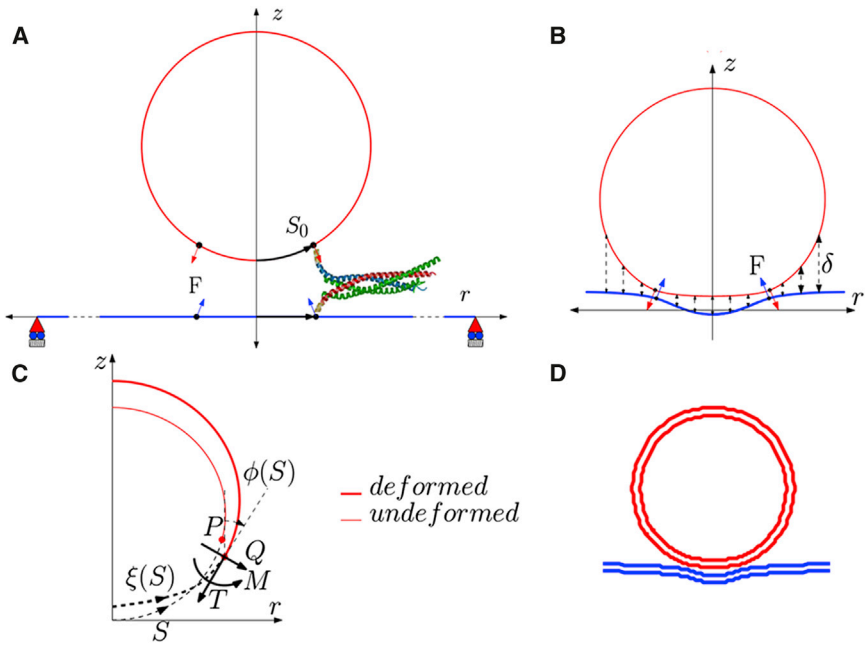

FIGURE 2 (*A*) A schematic of the axisymmetric model in the undeformed configuration showing the location of SNARE and direction of force applied. (*B*) The repulsive forces (shown by the *dotted lines*) act on the deformed configuration of the vesicle, as does the SNARE force, *F*. (*C*) The figure shows the convention for shear force (Q) in-plane tension (T) and moment (M) acting on the cross section of the membrane at location $\xi(S)$, where $\phi(S)$ is the tangent angle in the undeformed configuration measured from the vertical. (*D*) Example of a deformed vesicle-plasma membrane complex for a 20-nm diameter vesicle docked by 15 SNAREs. To see this figure in color, go online.

Local electrostatic interaction is determined by solving the Debye-Huckel equation for two infinite parallel planes separated by δ. We consider two limiting scenarios.

1. The membranes have fixed charge density throughout the process of docking, which corresponds to the case when the lipid molecules are completely ionized and have a fixed charge.
2. The membranes have fixed surface potential, which is achieved by adjusting the surface charge density of the ions in the Stern layer of the membrane or by varying the degree of ionization of the polarizable lipid molecules.

For the constant surface charge densities, the repulsive force along the z direction per unit area is given by

$$F_e = \frac{\sigma_1^2 + \sigma_2^2 + 2\sigma_1\sigma_2 \cosh(\delta/l_D)}{2\varepsilon\varepsilon_0 \sinh^2(\delta/l_D)}, \qquad (10)$$

where σ_1 andσ_2 are the surface charge densities of the vesicle and neuron base, respectively; l_D is the Debye length; ε is the relative permittivity of water; and ε_0 is the permittivity of vacuum. The choice of surface charge σ_1 is based on the force-displacement measurement by Marra (37) and the electrophoretic measurement by Ohsawa et al. (38). The reported value of surface charge is in the range 0.01–0.03 C/m^2. Also, assuming the same surface charge density on the outer leaflet of the plasma membrane and based on the observation by Pekker and Shneider (39) that a charge density difference of only ~0.0001 C/m^2 between the inner and outer leaflet is necessary to maintain the resting potential difference of 70 mV for the neuron cell, we choose the value of $\sigma_1 = \sigma_2 = -0.025$ C/m^2.

For the case of constant surface potential, the force per unit area is

$$F_e = \frac{l_D^2}{2\varepsilon\varepsilon_0} \frac{-\varphi_1^2 - \varphi_2^2 + 2\varphi_1\varphi_2 \cosh(\delta/l_D)}{\sinh^2(\delta/l_D)}. \qquad (11)$$

When the two membrane structures are far away from each other, they have charge density given as $\sigma_1 = \sigma_2 = -0.025$ C/m^2. The potentials on an isolated surface and charge density are related by

$$\varphi = \frac{l_D\sigma}{\varepsilon\varepsilon_0}. \qquad (12)$$

The value of surface potential for the bilayers, $\phi_1 = \phi_2 = -25$ mV, is evaluated using Eq. 12. As the vesicle approaches the membrane, the surface potential is held constant and Eq. 11 is used to obtain the force between the membranes. A similar approach was followed in Bykhovskaia et al. (11). However, in that work the mechanics of SNARE opening was not coupled to the electrostatic repulsion, and the SNARE-end opening was picked at 1 nm, whereas here the minimum separation of SNARE-ends is taken to be 2 nm. Primarily for this reason, the repulsive electrostatic forces in this work are in the range of tens of picoNewtons instead of the hundreds of picoNewtons quoted in Bykhovskaia et al. (11). Relevant parameters for modeling electrostatic forces are listed in Table S3.

Governing equations for the continuum membrane model and their solution

The vesicle-membrane system has been modeled under axisymmetry in an (r,θ,z) coordinate system. In the undeformed configuration, the vesicle is modeled as a sphere with radius R, whereas the undeformed plasma membrane is a circular disk of radius $L >> R$. As shown in Fig. 2, S refers to the undeformed arc length, whereas in the deformed configuration, the arc length is denoted by ξ. The tangent to the membrane makes an angle ϕ with the z axis and the mean curvature of the membrane surfaces is denoted by H.

The forces in the membranes are shear force, Q and the in-plane tension, T as shown in Fig. 2 *C*. The osmotic pressure inside the synaptic vesicle is represented by p_0. As shown in Fig. 2 *B*, the repulsive electrostatic force per unit area, F_e in Eqs. 9 and 10, acts on both membranes, along the z direction. The force due to SNARE bundles is represented as line loads acting on the circles over the undeformed geometry of vesicle and plasma membrane (denoted by vectors F and $-F$, as shown in Fig. 2 *B*). On the vesicle, the radius of this circle, r_0, is determined by the geometrical compatibility condition, which is based on the width of SNARE helix, d and number of SNARE bundles, as

$$r_0 = \frac{(\text{number of SNAREs}) \times d}{2\pi}. \qquad (13)$$

The assumption here is that the packing of SNAREs is limited by steric hindrance between them and Eq. 13 represents the smallest radius that would accommodate the given number of bundles. The equivalent arc length value for load application is given by $S_0 = \sin^{-1}(r_0/R)$. This arc length is same for both the vesicle and the membrane.

We assume that the strain energy density W of both membranes is given by (40)

$$W = c\ H^2 \tag{14}$$

and by variation of total energy, the governing equations for the vesicle-membrane system are obtained in Eq. S11 in the Supporting Material. These equations represent equilibrium in the normal (Eq. S11 *a* in the Supporting Material) and tangential (Eq. S11 *f* in the Supporting Material) directions at each point on the membranes. The geometrical constraints can be used to obtain Eqs. S11, *b-e*, in the Supporting Material. These governing equations form a nonlinear system of ordinary differential equations (ODEs). By specifying the input geometric parameters (R,L) and the force parameters (F, S_0, F_e, and p_0), this system of ODEs can be solved numerically to obtain an equilibrium configuration of the membrane system. We use the nonlinear boundary value problem solver BVP4C in the software MATLAB (The MathWorks, Natick, MA) to solve the ODEs.

RESULTS AND DISCUSSION

Force-displacement response of the vesicle-membrane interaction

The equal and opposite forces on the Syx and Syb C-termini are transmitted to the plasma membrane and vesicle, respectively, as forces attracting them. Below separations of ~2.5 nm, attractive forces are resisted primarily by hydration repulsion. A characteristic force-separation curve can be obtained for the vesicle-membrane system using the formulation described in Continuum Model of the Vesicle and Plasma Membrane. By specifying the number of SNARE bundles attached to the vesicle-membrane system, the location of the line load can be determined using Eq. 13. The effect of zipping of the SNARE bundle is simulated by varying the strength of the line load in small steps. For each increment in force, an equilibrium configuration of the membrane system is obtained, and hence we determine the separation between the two load points on vesicle and plasma membrane, respectively. This separation is the distance between residues Syb89 and Syx256. By varying the number of SNAREs, a series of force-separation curves can be obtained as shown in Fig. 3 *A*.

SNARE force-separation curve

Fig. 3 *B* shows the results of a simulation in which the SNARE bundle has been pulled apart for a total end-to-end separation of 20 nm between the C-terminal Syb and Syx end-beads.

Each drop in the force-displacement plot (Fig. 3 *B*) represents the system overcoming a barrier where there is a strong interaction between the SNARE bundles. Two examples are the snapshots at 10.9 and 11.9 nm in Fig. 3 *B*. With an increase of only 1.0 nm in displacement and little visible change in structure, there is a significant (5.1 pN) increase in force to a peak value of 17.2 pN, after which the force immediately drops to ~2 pN. (Because a significant amount of the linker domain was not present in the crystal structure of SNARE that was used to build the CG model, the first force jump seen by Gao et al. (8) at 3 nm and 8–13 pN is

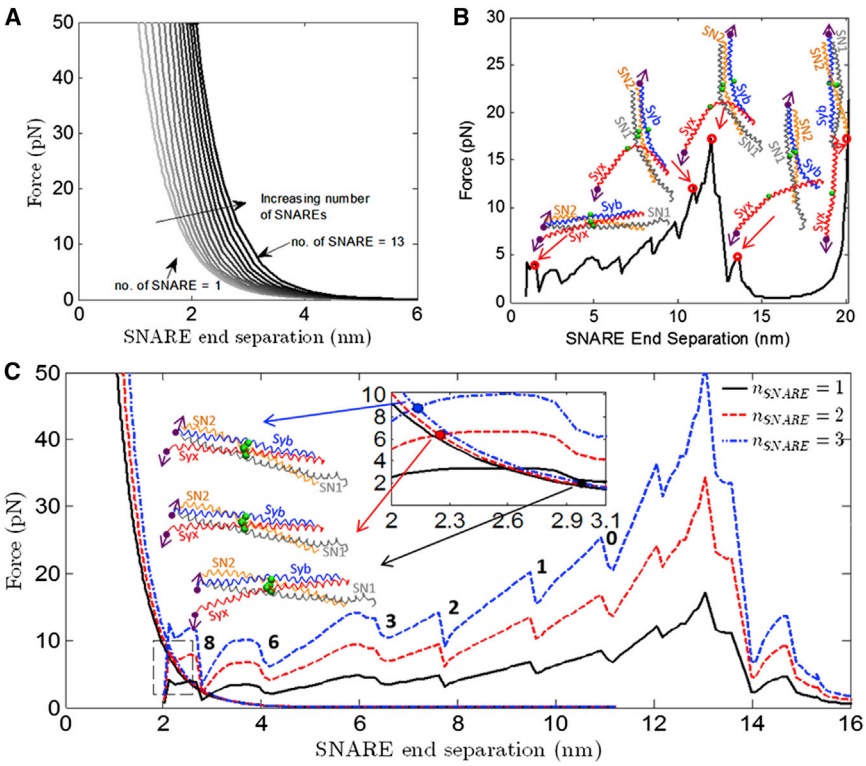

FIGURE 3 (*A*) Force versus SNARE end separation for the vesicle-membrane system for different numbers of SNAREs for the hydration repulsion case. (*B*) The force during separation of the ends of the SNARE bundle using λ of 0.30 for the CG model of SNARE along with snapshots of the SNARE bundle at the corresponding C-terminal end separation. The end separation is defined as the distance between the Syb and Syx C-terminal beads Syb89 and Syx256. Syb, Syx, the ionic layer residues (*beads*), and the C-terminal residues (*beads with arrows*) that are attached to pulling beads are shown in each SNARE snapshot. (*Arrows*) Direction along which the C-terminal beads are being pulled. (*C*) The force as a function of Syb-Syx C-terminal distance (between Syb89 and Syx256) is shown for the vesicle-membrane (the exponentially decreasing curves) and SNARE. One (*solid line*), two (*dash line*), and three (*dash-dot line*) SNAREs are shown in this plot. Intersections between the vesicle-membrane and SNARE force-displacement responses represent equilibrium states. There are a number of instabilities represented by load-drops. These correspond to separation of individual layers, and have been so-labeled. To see this figure in color, go online.

not present in these results.) The CG model is able to capture the experimentally determined precipitous force-drop, after which the remaining interactions holding the SNARE bundle together are relatively weak and are therefore not measurable in a force-controlled experiment.

The subsequent increase in force is associated with stretching of the linkage between the N-termini of Syx and Syb, and presumably would not be present in a physiological setting. It is included here because this feature is also present in the experiments of Gao et al. (8). For simplicity, in the version of the elastic network model used here, we do not allow the helices to unravel, justified by the following facts. As the results of the next section show, the equilibrium separation for all the cases studied in this article is ~3 nm or less. At these separations, the force on each SNARE is <5 pN. Based on the work of Gao et al. (8), the first unwinding event occurs at ~10–12 pN. Thus our simplifying assumption (which will be relaxed in future work) that helices remain unfolded, is justifiable for the range of openings and displacements representative of the equilibrium docked state. We have checked the sensitivity of our results to this assumption by allowing small portions of the unzippered region to unfold, as shown in the Supporting Material.

Combined SNARE and vesicle-membrane results

In the previous two sections we have independently obtained force-separation results for the vesicle-membrane system (Fig. 3 *A*) and for the SNARE (Fig. 3 *B*). Before combining the two results, we first accounted for the fact that the distance between outer surfaces of the membranes is larger by ~2 nm than the distance between Syb89 and Syx256, the SNARE residues that we move apart (see the Supporting Material). Specifically, we shifted the SNARE force-displacement curve to the right by 2 nm to obtain this consistency. Clearly, in the combined SNARE-vesicle-membrane system there is a single force and corresponding displacement. Applying this consistency condition between the two results determines equilibrium. Moreover, we can determine how equilibrium depends on the number of SNARES.

For systems with 1, 2, and 3 SNAREs, the information from Fig. 3, *A* and *B*, is combined to produce Fig. 3 *C*. Because it has been shown that SNAREs mediate vesicle to membrane fusion in a synchronous way, we assume that the force required to unzip two SNAREs would simply be twice the force required to unzip one SNARE, and so on (41,42). In all three cases, the curves intersect at an equilibrium SNARE end separation of between 2 and 3 nm, suggesting that even 1–3 SNAREs are sufficient to overcome hydration repulsion and allow the vesicle to dock at the plasma membrane. The corresponding structures for the intersection points for all three cases, shown in Fig. 3 *C*, also suggest there is no important conformational difference between the three structures other than a difference in the number of residues that have been unzippered.

It is instructive next to consider the energy landscape corresponding to the force-separation results shown in Fig. 3. For this purpose, the SNARE (positive) and vesicle-membrane (negative) force-separation results are integrated numerically. Fig. 4 *B* shows the results corresponding to

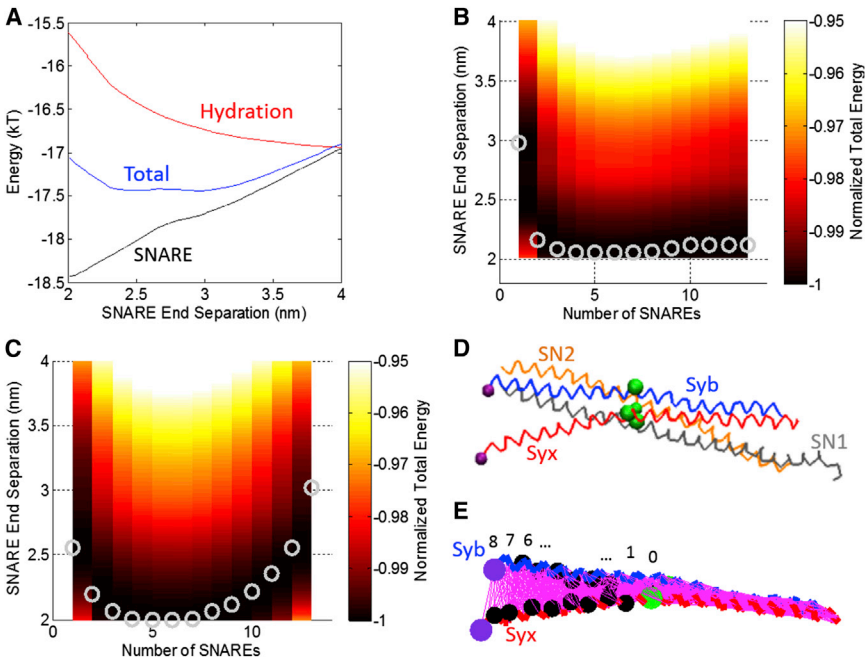

FIGURE 4 (*A*) Energy as a function of SNARE end separation when repulsion between the vesicle and plasma membrane is dominated by hydration repulsion. The energetic contributions from SNARE (attractive), hydration (repulsive), and the total (their sum) are shown. The hydration repulsion has been shifted vertically by −17 kT for clarity. (*B*) Contour plot of total energy as a function of SNARE end separation distance for different numbers of SNAREs under hydration repulsion. (*Circles*) Global energy minima representing the equilibrium SNARE end separation for a given number of SNAREs. Vesicle radius is 20 nm. (*C*) Contour plot of total energy as a function of SNARE end separation distance for different numbers of SNAREs under electrostatic repulsion for a fixed charge of −0.025 C/m^2 on the vesicle and the membrane in the limit of high tension in the vesicle and plasma membrane. For this case, minimum lateral separation between the SNARE bundles has been increased from 3 to 4 nm. (*D*) The structure of SNARE corresponding to the case shown in (*B*), number of SNAREs = 1. Syb, Syx, SN1, and SN2 are shown with the ionic layer residues indicated as large beads. (*E*) The same structure as in (*D*) but showing only Syb and Syx for clarity. (*Thin lines*) All contacts for residues within 2σ of each other. To see this figure in color, go online.

the force-separation results shown in Fig. 3. Note that because the SNARE force-displacement response contains unstable jumps, the entire energy landscape is not represented in Fig. 4, *B* and *C*. Because of the nature of the displacement control simulations, there are several instabilities present in the original SNARE force-separation curve. An example of one of these instabilities is the drop at 7.5 nm, as shown in the SNARE curves in Fig. 3 *C*. Integrating across these instabilities makes the total energy of the system slightly more negative than it should be (see the Supporting Material). Fig. 4, *B* and *C*, shows contour plots of interaction energy as a function of the number of SNAREs and end-to-end separation. Fig. 4 *B* shows the results for a vesicle with radius of 20 nm, representing a synaptic vesicle. The gray circles represent the global energy minimum for each value of number of SNARES, corresponding to force equilibria in Fig. 3.

An example of how these minima were determined is shown in Fig. 4 *A*. This was used to determine the global energy minimum for one SNARE for the hydration repulsion case. It is striking that a single SNARE produces a distinct energy minimum at ~3 nm. As the number of SNAREs increases to four SNAREs, the equilibrium SNARE end-separation decreases. For 4–8 SNAREs, there is little difference in the equilibrium separation. For five SNAREs, the total energy per SNARE is ~−17 kT, which is quite consistent with the 13–27 kT range reported by Zorman et al. (43). With increase in the number of SNAREs over 8, the equilibrium SNARE separation slowly increases; the minimum separation (~2.1 nm) is achieved with four bundles. Thus, we may conclude that 4–8 SNAREs are sufficient to complete the zippering process and to bring the membrane and the vesicle at a distance of 2.1 nm. Importantly, a larger number of SNARE bundles does not bring the vesicle closer to the membrane, because steric hindrance pushes them out to a larger radius.

We next explored how electrostatics would affect the vesicle-to-plasma membrane repulsion. We recalculated the continuum model results using a fixed surface charge of -0.025 C/m^2 on the vesicle and the membrane with electrostatic repulsion as shown in Fig. S9 *B*. For this case for one SNARE, the end separation is ~2.4 nm, which is smaller than the 3 nm seen for the hydration repulsion case. However, when more than one SNARE is added to the system, the equilibrium SNARE end separation is constant at ~2 nm for 2–13 SNAREs. In this case, the equilibrium configuration of the SNARE bundle would be a nearly completely zipped conformation. For this case with four SNARES the total energy per SNARE is ~−14 kT, which again is within the range of 13–27 kT reported by Zorman et al. (43).

We next explored how the vesicle size would affect the number of SNAREs required to dock a vesicle to the membrane. Fig. S10, *B* and *D*, shows the results for the case of a vesicle that is 100 nm in radius, corresponding to vesicles in neurosecretory cells. For the hydration repulsion case, there is a considerable difference between the 20- and 100-nm vesicles. For the 100-nm case the minimum separation is also reached with four SNAREs, but that minimum separation is ~2.5 nm as opposed to ~2.1 nm for the 20-nm vesicle. For the case of electrostatic repulsion with a constant surface charge, the only difference between the two cases is for one and two SNAREs. For the 100-nm vesicle case, the equilibrium separation is ~3.4 nm as opposed to ~2.4 nm for the 20-nm vesicle. Additionally, for two SNAREs, there is also a larger separation for the 100-nm vesicle of 3 nm as opposed to 2 nm for the 20-nm vesicle. However for three or more SNAREs, there is little difference between the two vesicle sizes because both SNARE configurations are nearly completely zippered.

Fig. 4, *B* and *C*, represents results for an optimized set of parameters describing molecular details and electrostatic forces. To judge the robustness of the conclusions gleaned from these results, we explored several variations of parameters, including: 1) allowing a portion of Syb to melt with the surface charge held constant; 2) holding the surface potential constant instead of surface charge; 3) high osmotic pressure in the vesicle and low pre-tension in the plasma membrane; and 4) the limit of high tension in both the vesicle and plasma membranes. These variations in the modeling assumptions generally make little difference in the conclusions drawn from Fig. 4 (see the Supporting Material for details). The main conclusion that 4–8 SNAREs bring the vesicle to the minimum distance away from the membrane still holds. Because the equilibria of interest for the problem addressed in this work occur at relatively small separation and forces, in our model we have not allowed the helices to unravel. In order to see the potential effect of unraveling, the first two helical turns of Syb were melted and the force-displacement curve for SNARE was calculated from Fig. 3 *B*. The resulting energy surface for this case for a 20-nm vesicle with hydration repulsion is shown in Fig. S11 *A*. A quantity of 4–10 SNAREs brings the vesicle within a minimal distance of the plasma membrane. However, that minimal distance is ~2.4 nm as opposed to the ~2.1 nm for the case where Syb is not permitted to unravel.

In an effort to compare to the experimental prefusion structures of the vesicle and plasma membrane as shown by Malsam et al. (44) and Hernandez et al. (45), the continuum model was calculated using high osmotic pressure in the vesicle and low pre-tension in the plasma membrane. However, the resulting energy surface for this modification to the base cases shown in Fig. 4 has little effect on the results because the repulsive force is dominated by hydrostatic repulsion as shown in Fig. S14.

The limit of high tension in both the vesicle and plasma membrane was studied using an analytical model described in the Supporting Material. In order to test the sensitivity of the solution to the location of the SNAREs, calculated using Eq. 13, the diameter of the SNARE bundle was varied from

2 nm, Fig. S17 *A*, to 4 nm, whereas the base case used 3 nm. This variation seems to have the most significant effect on the solution. Decreasing the size of the SNARE bundle still yields similar results, in that for more than one SNARE, the bundle is nearly completely zipped shut. On the other hand, when the size of the SNARE bundle is increased, instead of having a nearly fully zippered bundle, there is a minimum separation that occurs at four SNAREs. With the addition of more than five SNAREs the equilibrium separation again begins to increase all the way up to ~3 nm with 13 SNAREs.

Fig. 4, *D* and *E*, shows the equilibrium structures of SNARE at a 2.1-nm separation for the case shown in Fig. 4 *B*. SN1 and SN2 were removed from the structure for clarity in Fig. 4 *E*, and the residues of Syb and Syx that were in contact were determined. Because the forces from Miyazawa and Jernigan (23–25) greatly decrease after a separation of ~2*σ, that distance was used as the criteria for two residues being in contact. At the start of the displacement control simulation, Syb and Syx had 574 contacts between them. After a 2.1-nm separation, only 449 contacts remained. The removed contacts begin to create a cracklike defect separating the helices. After the 2.1-nm separation, residues 89 (Trp) of Syb and 256 (Lys) of Syx were still in contact. These residues are still far away from the ionic layer, showing that the SNARE bundle had not yet unzipped to that point.

CONCLUSIONS

The docking of vesicles onto the plasma membrane of a neuron involves interplay between the SNARE complexes that provide attractive forces, long-range repulsion between the vesicle and membrane, and deformation of all three components. Although each of these components has previously been investigated in detail, to understand the biophysics and mechanics of vesicle docking, it is imperative to combine them. To our knowledge, we report the first model to couple chemical specificity of the SNARE complex with hydration, electrostatic, and mechanical forces imposed on the vesicle and plasma membrane. Such a model can serve as a tool to investigate how mutations in the SNARE complex could affect the docking and fusion process.

We have developed separate coarse-grained models for the deformation of the SNARE complex and of the vesicle-membrane assembly. The vesicle-membrane model is based on a continuum description of membrane deformation subjected to either hydration or electrostatic repulsion and forces from the SNARE complexes. The fusion of lipid bilayers has been extensively modeled (46) to capture the intermediate states of fusion, including stalk formation, and to understand their energetics. Our goal in this study was to understand the forces produced by membrane bending and hydration or electrostatic repulsion that need to be overcome by the SNARE complexes to dock a vesicle to the membrane. The continuum membrane model was coupled with a coarse-grained model of the SNARE complex. The SNARE forces are represented in the continuum membrane model as an axisymmetric line force, an assumption that is increasingly accurate for increasing number of SNAREs. (A single SNARE at the axis of symmetry also presumably results in axisymmetric deformations of the vesicle/membrane.) For a given number of SNARES, the model holds fixed their anchor points in the vesicle and plasma membrane. This constraint potentially affects our results. However, we note that the position of the SNARE anchor points does vary as we change the number of SNAREs (Eq. 13). The number of SNAREs was varied from 1 to 13. Usually, for two or more SNAREs there is little difference in the equilibrium separation, suggesting that the model results probably will not vary much if we remove the constraint of holding the positions fixed.

The CG SNARE model is based on an elastic-network representation of each of the helices combined with potentials from Miyazawa and Jernigan (23–25) to capture interhelical interactions. It is a minimalistic model that still represents residue-specificity. Its few parameters are calibrated either by comparison with all-atom MD simulations of individual SNAREs, or by comparison to experimentally measured forces to separate a single SNARE complex (8) Specifically, we match the experimentally observed peak force of 17.2-pN force. Each of the two models separately yields a force-separation relationship. Enforcing consistency between the two yields equilibrium configurations for the SNARE-vesicle-membrane complex for a given number of SNAREs.

As the first application of our model, we explored here the effect of the number of SNARE complexes on the mechanics of vesicle docking and the prefusion state of the SNARE complex. It is still a matter of debate as to how many SNARE complexes need to assemble before the fusion process. High concentration of Syb on the vesicle (~70 copies (47)), as well t-SNARE clusters at docking sites (48) suggest that in vivo fusion may be mediated by multiple SNARE complexes. At the same time, experiments and model systems suggest that one (49), two (18), or three (19,50,51) could be sufficient. Other studies, however, suggest a larger number of SNARE complexes per fusion, ranging between 5 and 11 (16,20,52). Finally, recent studies suggest that the number of assembled SNARE complexes may determine the release efficiency (53) and that it may vary (54). Thus, how vesicle docking might depend on the number of SNARE complexes remains an open question, previously not addressed from the biophysical and biomechanical point of view.

We find that one SNARE complex is sufficient to dock the vesicle onto the membrane. As few as 2–3 SNAREs are sufficient to bring the distance between the membrane and vesicle to the minimum and thus to complete the docking process. Interestingly, there is a point of diminishing returns

such that a larger number of SNAREs (i.e., an overdocked state) does not further reduce the vesicle-membrane separation. The corresponding predicted SNARE end-to-end separation is in the range 2–3 nm (55,56), but one can expect significant fluctuation about the equilibrium state because the energy profile is relatively shallow (Fig. 4 *A*). This picture of a partially zippered docked state is consistent with the conclusions of an in vivo toxin cleavage assay in crayfish neuromuscular junctions. In this work, we only model docking, not fusion. That is, we calculate the equilibrium separation between the vesicle and plasma membrane during docking. The lower bound of ~2-nm separation between the vesicle and plasma membrane is based on the steric hindrance of having to fit the SNARE bundles between the two surfaces. This distance is probably a bit too large for fusion to occur, which suggests that some additional mechanism other than SNARE zippering must act for fusion.

Several variations in the model including calculations under fixed charge, fixed surface potential, high vesicle pressure, high membrane tension, and varying vesicle radius, have all shown similar results.

Our results are consistent with the view that a prefusion state involves a partially assembled SNARE complex (57–59), which keeps the vesicle at a short distance from the plasma membrane in anticipation of Ca^{2+}-induced fusion rather than the alternative view that SNARE zippering represents a final step of exocytosis and rapidly progresses once nucleated (60). Specifically, our model robustly predicts an equilibrium separation between the vesicle and the membrane to be of ~2.0–3.0 nm corresponding to opening of, at most, layer 8.

SUPPORTING MATERIAL

Supporting Material, 17 figures, three tables, and 19 equations are available at http://www.biophysj.org/biophysj/supplemental/S0006-3495(15)00341-0.

AUTHOR CONTRIBUTIONS

N.F. and A.J. developed the CG SNARE model; N.F. wrote the CG SNARE model code; and P.S. and C.-Y.H. developed the continuum model of the vesicle and plasma membrane. All authors analyzed and interpreted results.

ACKNOWLEDGMENTS

The authors gratefully acknowledge several useful suggestions by Professor Jeetain Mittal.

This study is supported by grant No. R01 MH099557 from the National Institutes of Health. For molecular-dynamics computations, we acknowledge the support of XSEDE, which is supported by National Science Foundation grant No. OCI-1053575, and specifically the Texas Advanced Computing Center under grant No. TG-MCB100049 and the National Institute of Computational Science. VMD/NAMD software is developed with National Institutes of Health support by the Theoretical and Computational Biophysics group at the Beckman Institute, University of Illinois at Urbana-Champaign, Urbana, IL.

SUPPORTING CITATIONS

References (61–68) appear in the Supporting Material.

REFERENCES

1. Südhof, T. C. 1995. The synaptic vesicle cycle: a cascade of protein-protein interactions. *Nature.* 375:645–653.
2. Hanson, P. I., J. E. Heuser, and R. Jahn. 1997. Neurotransmitter release—four years of SNARE complexes. *Curr. Opin. Neurobiol.* 7:310–315.
3. Söllner, T., M. K. Bennett, …, J. E. Rothman. 1993. A protein assembly-disassembly pathway in vitro that may correspond to sequential steps of synaptic vesicle docking, activation, and fusion. *Cell.* 75:409–418.
4. Rothman, J. E. 1994. Mechanisms of intracellular protein transport. *Nature.* 372:55–63.
5. Gracheva, E. O., E. B. Maryon, …, J. E. Richmond. 2010. Differential regulation of synaptic vesicle tethering and docking by UNC-18 and TOM-1. *Front. Synaptic Neurosci.* 2:141.
6. Sutton, R. B., D. Fasshauer, …, A. T. Brunger. 1998. Crystal structure of a SNARE complex involved in synaptic exocytosis at 2.4 Å resolution. *Nature.* 395:347–353.
7. Ernst, J. A., and A. T. Brunger. 2003. High resolution structure, stability, and synaptotagmin binding of a truncated neuronal SNARE complex. *J. Biol. Chem.* 278:8630–8636.
8. Gao, Y., S. Zorman, …, Y. Zhang. 2012. Single reconstituted neuronal SNARE complexes zipper in three distinct stages. *Science.* 337:1340–1343.
9. Durrieu, M.-P., R. Lavery, and M. Baaden. 2008. Interactions between neuronal fusion proteins explored by molecular dynamics. *Biophys. J.* 94:3436–3446.
10. Bock, L. V., B. Hutchings, …, D. J. Woodbury. 2010. Chemomechanical regulation of SNARE proteins studied with molecular dynamics simulations. *Biophys. J.* 99:1221–1230.
11. Bykhovskaia, M., A. Jagota, …, J. T. Littleton. 2013. Interaction of the complexin accessory helix with the C-terminus of the SNARE complex: molecular-dynamics model of the fusion clamp. *Biophys. J.* 105:679–690.
12. Durrieu, M. P., P. J. Bond, …, M. Baaden. 2009. Coarse-grain simulations of the R-SNARE fusion protein in its membrane environment detect long-lived conformational sub-states. *ChemPhysChem.* 10:1548–1552.
13. Lindau, M., B. A. Hall, …, M. S. P. Sansom. 2012. Coarse-grain simulations reveal movement of the synaptobrevin C-terminus in response to picoNewton forces. *Biophys. J.* 103:959–969.
14. Marrink, S. J., H. J. Risselada, …, A. H. de Vries. 2007. The MARTINI force field: coarse-grained model for biomolecular simulations. *J. Phys. Chem. B.* 111:7812–7824.
15. Lamberg, A., and T. Taniguchi. 2014. Coarse-grained computational studies of supported bilayers: current problems and their root causes. *J. Phys. Chem. B.* 118:10643–10652.
16. Han, X., C.-T. Wang, …, M. B. Jackson. 2004. Transmembrane segments of syntaxin line the fusion pore of Ca^{2+}-triggered exocytosis. *Science.* 304:289–292.
17. van den Bogaart, G., and R. Jahn. 2011. Counting the SNAREs needed for membrane fusion. *J. Mol. Cell Biol.* 3:204–205.
18. Sinha, R., S. Ahmed, …, J. Klingauf. 2011. Two synaptobrevin molecules are sufficient for vesicle fusion in central nervous system synapses. *Proc. Natl. Acad. Sci. USA.* 108:14318–14323.
19. Mohrmann, R., H. de Wit, …, J. B. Sorensen. 2010. Fast vesicle fusion in living cells requires at least three SNARE complexes. *Science.* 330:502–505.

20. Karatekin, E., J. Di Giovanni, …, J. E. Rothman. 2010. A fast, single-vesicle fusion assay mimics physiological SNARE requirements. *Proc. Natl. Acad. Sci. USA.* 107:3517–3521.

21. Zhang, Z., J. Pfaendtner, …, G. A. Voth. 2009. Defining coarse-grained representations of large biomolecules and biomolecular complexes from elastic network models. *Biophys. J.* 97:2327–2337.

22. Chu, J. W., and G. A. Voth. 2006. Coarse-grained modeling of the actin filament derived from atomistic-scale simulations. *Biophys. J.* 90:1572–1582.

23. Miyazawa, S., and R. L. Jernigan. 1985. Estimation of effective inter-residue contact energies from protein crystal structures: quasi-chemical approximation. *Macromolecules.* 18:534–552.

24. Miyazawa, S., and R. L. Jernigan. 1996. Residue-residue potentials with a favorable contact pair term and an unfavorable high packing density term, for simulation and threading. *J. Mol. Biol.* 256:623–644.

25. Miyazawa, S., and R. L. Jernigan. 1999. Self-consistent estimation of inter-residue protein contact energies based on an equilibrium mixture approximation of residues. *Proteins.* 34:49–68.

26. Jenkins, J. T. 1977. Static equilibrium configurations of a model red blood cell. *J. Math. Biol.* 4:149–169.

27. Long, R., C. Y. Hui, …, M. Bykhovskaia. 2012. Adhesion energy can regulate vesicle fusion and stabilize partially fused states. *J. R. Soc. Interface.* 9:1555–1567.

28. Hess, B., C. Kutzner, …, E. Lindahl. 2008. GROMACS 4: algorithms for highly efficient, load-balanced, and scalable molecular simulation. *J. Chem. Theory Comput.* 4:435–447.

29. Foloppe, N., and A. D. MacKerell. 2000. All-atom empirical force field for nucleic acids: I. Parameter optimization based on small molecule and condensed phase macromolecular target data. *J. Comput. Chem.* 21:86–104.

30. Alberts, B., A. Johnson, …, P. Walter. 2002. Molecular Biology of the Cell, 4th Ed. Garland Science, New York.

31. Creighton, T. E. 1993. Proteins: Structures and Molecular Properties, 2nd Ed. W. H. Freeman, New York.

32. Kim, Y. C., and G. Hummer. 2008. Coarse-grained models for simulations of multiprotein complexes: application to ubiquitin binding. *J. Mol. Biol.* 375:1416–1433.

33. Argento, C., A. Jagota, and W. C. Carter. 1997. Surface formulation for molecular interactions of macroscopic bodies. *J. Mech. Phys. Solids.* 45:1161–1183.

34. McIntosh, T. J., A. D. Magid, and S. A. Simon. 1990. Interactions between charged, uncharged, and zwitterionic bilayers containing phosphatidylglycerol. *Biophys. J.* 57:1187–1197.

35. Aeffner, S., T. Reusch, …, T. Salditt. 2012. Energetics of stalk intermediates in membrane fusion are controlled by lipid composition. *Proc. Natl. Acad. Sci. USA.* 109:E1609–E1618.

36. McIntosh, T. J., and S. A. Simon. 1994. Hydration and steric pressures between phospholipid bilayers. *Annu. Rev. Biophys. Biomol. Struct.* 23:27–51.

37. Marra, J. 1986. Direct measurement of the interaction between phosphatidylglycerol bilayers in aqueous electrolyte solutions. *Biophys. J.* 50:815–825.

38. Ohsawa, K., M. Murata, and H. Ohshima. 2005. Zeta potential and surface charge density of polystyrene-latex; comparison with synaptic vesicle and brush border membrane vesicle. *Colloid Polym. Sci.* 264:1005–1009.

39. Pekker, M., and M. N. Shneider. 2014. The surface charge of a cell lipid membrane. *arXiv Prepr.* arXiv. 1401–1407.

40. Cooke, I. R., and M. Deserno. 2005. Solvent-free model for self-assembling fluid bilayer membranes: stabilization of the fluid phase based on broad attractive tail potentials. *J. Chem. Phys.* 123:224710.

41. Risselada, H. J., C. Kutzner, and H. Grubmüller. 2011. Caught in the act: visualization of SNARE-mediated fusion events in molecular detail. *ChemBioChem.* 12:1049–1055.

42. Risselada, H. J., and H. Grubmüller. 2012. How SNARE molecules mediate membrane fusion: recent insights from molecular simulations. *Curr. Opin. Struct. Biol.* 22:187–196.

43. Zorman, S., A. A. Rebane, …, Y. Zhang. 2014. Common intermediates and kinetics, but different energetics, in the assembly of SNARE proteins. *eLife.* 3:e03348.

44. Malsam, J., D. Parisotto, …, T. H. Söllner. 2012. Complexin arrests a pool of docked vesicles for fast Ca^{2+}-dependent release. *EMBO J.* 31:3270–3281.

45. Hernandez, J. M., A. Stein, …, R. Jahn. 2012. Membrane fusion intermediates via directional and full assembly of the SNARE complex. *Science.* 336:1581–1584.

46. Chernomordik, L. V., and M. M. Kozlov. 2008. Mechanics of membrane fusion. *Nat. Struct. Mol. Biol.* 15:675–683.

47. Takamori, S., M. Holt, …, R. Jahn. 2006. Molecular anatomy of a trafficking organelle. *Cell.* 127:831–846.

48. Knowles, M. K., S. Barg, …, W. Almers. 2010. Single secretory granules of live cells recruit syntaxin-1 and synaptosomal associated protein 25 (SNAP-25) in large copy numbers. *Proc. Natl. Acad. Sci. USA.* 107:20810–20815.

49. van den Bogaart, G., M. G. Holt, …, R. Jahn. 2010. One SNARE complex is sufficient for membrane fusion. *Nat. Struct. Mol. Biol.* 17:358–364.

50. Hua, Y., and R. H. Scheller. 2001. Three SNARE complexes cooperate to mediate membrane fusion. *Proc. Natl. Acad. Sci. USA.* 98:8065–8070.

51. Shi, L., Q.-T. Shen, …, F. Pincet. 2012. SNARE proteins: one to fuse and three to keep the nascent fusion pore open. *Science.* 335:1355–1359.

52. Megighian, A., M. Zordan, …, C. Montecucco. 2013. Evidence for a radial SNARE super-complex mediating neurotransmitter release at the *Drosophila* neuromuscular junction. *J. Cell Sci.* 126:3134–3140.

53. Acuna, C., Q. Guo, …, T. C. Südhof. 2014. Microsecond dissection of neurotransmitter release: SNARE-complex assembly dictates speed and Ca^{2+} sensitivity. *Neuron.* 82:1088–1100.

54. Hernandez, J. M., A. J. B. Kreutzberger, …, R. Jahn. 2014. Variable cooperativity in SNARE-mediated membrane fusion. *Proc. Natl. Acad. Sci. USA.* 111:12037–12042.

55. Prashad, R. C., and M. P. Charlton. 2014. SNARE zippering and synaptic strength. *PLoS ONE.* 9:e95130.

56. Hua, S. Y., and M. P. Charlton. 1999. Activity-dependent changes in partial VAMP complexes during neurotransmitter release. *Nat. Neurosci.* 2:1078–1083.

57. Sørensen, J. B., K. Wiederhold, …, D. Fasshauer. 2006. Sequential N- to C-terminal SNARE complex assembly drives priming and fusion of secretory vesicles. *EMBO J.* 25:955–966.

58. Walter, A. M., K. Wiederhold, …, J. B. Sørensen. 2010. Synaptobrevin N-terminally bound to syntaxin-SNAP-25 defines the primed vesicle state in regulated exocytosis. *J. Cell Biol.* 188:401–413.

59. Li, F., D. Kümmel, …, F. Pincet. 2014. A half-zippered SNARE complex represents a functional intermediate in membrane fusion. *J. Am. Chem. Soc.* 136:3456–3464.

60. Jahn, R., and D. Fasshauer. 2012. Molecular machines governing exocytosis of synaptic vesicles. *Nature.* 490:201–207.

61. Schlick, T. 2002. Molecular Modeling and Simulation: An Interdisciplinary Guide. Springer, New York.

62. Kubo, R. 2002. The fluctuation-dissipation theorem. *Rep. Prog. Phys.* 29:255–284.

63. Ohsawa, K., H. Ohshima, and S. Ohki. 1981. Surface potential and surface charge density of the cerebral-cortex synaptic vesicle and stability of vesicle suspension. *Biochim. Biophys. Acta.* 648: 206–214.

64. Deserno, M. 2007. Fluid Lipid Membranes—a Primer. http://www.cmu.edu/biolphys/deserno/pdf/membrane_theory.pdf.

65. Kweon, D. H., C. S. Kim, and Y. K. Shin. 2002. The membrane-dipped neuronal SNARE complex: a site-directed spin labeling electron paramagnetic resonance study. *Biochemistry.* 41:9264–9268.

66. Kweon, D.-H., C. S. Kim, and Y.-K. Shin. 2003. Regulation of neuronal SNARE assembly by the membrane. *Nat. Struct. Biol.* 10:440–447.

67. Kim, C. S., D. H. Kweon, and Y. K. Shin. 2002. Membrane topologies of neuronal SNARE folding intermediates. *Biochemistry.* 41:10928–10933.

68. Stein, A., G. Weber, …, R. Jahn. 2009. Helical extension of the neuronal SNARE complex into the membrane. *Nature.* 460: 525–528.

Coarse-Grained Model of SNARE Mediated Docking

Nicole Fortoul,[†] Pankaj Singh,[‡] Chung-Yuen Hui,[‡] Maria Bykhovskaia,[§] Anand Jagota,[†¶]

[†]Department of Chemical and Biomolecular Engineering and [¶]Bioengineering Program, Lehigh University, Bethlehem PA 18017
[‡]Department of Mechanical & Aerospace Engineering, Cornell University, Ithaca, NY 14853
[§]Neuroscience Department, Universidad Central del Caribe, Bayamon, Puerto Rico

SUPPORTING MATERIAL

1. Coarse grain simulations: solution procedure

CG simulations were conducted for the 4 individual helices using Langevin dynamics at 300 K for a range of values of k_s. The Langevin equation (1) includes an inertial term, a viscous term, a random force term, and a potential energy term, respectively, in the form

$$m\ddot{x}(t) = -\gamma\dot{x}(t) + R(t) - \nabla E \tag{S1}$$

where m is the mass of each bead, $\ddot{x}(t)$ is the bead's acceleration at time t, γ is the damping constant, $\dot{x}(t)$ is the bead's velocity at t, $R(t)$ is a random force that represents the protein's interaction with the surrounding fluid, and E is the potential energy governing the solute that includes ENM forces. The fluctuation-dissipation theorem (2) connects the random force and viscous drag

$$\left\langle R(t)\cdot R(t')\right\rangle = 6\gamma k_B T\delta(t-t') \tag{S2}$$

where k_B is Boltzman's constant, T is temperature, $R(t')$ is the random force applied at t', and $\delta(t-t')$ is the Dirac delta function. Written as a system of equations for all beads, the Langevin equation takes the form

$$[M]\{\ddot{u}(t)\} = -\gamma\{\dot{u}(t)\} + \{R(t)\} - [k]\{u(t)\} \tag{S3}$$

where $[M]$ is a diagonal mass matrix, $\{\ddot{u}(t)\}, \{\dot{u}(t)\}, and\ \{u(t)\}$ are column vectors containing the accelerations, velocities, and positions in the x, y, and z directions for each bead, $\{R(t)\}$ is a column vector containing the random force in the x, y, and z directions for each bead, and $[k]$ is a stiffness matrix.

The standard deviation of the random force is derived from Eqs. S2 and S3 to be

$$SD = \sqrt{\frac{2m\gamma k_B T}{\Delta t}} \tag{S4}$$

where Δt is the timestep. The friction coefficient is dependent on the bead type as well

$$\gamma = \frac{6\pi\eta a}{m} \tag{S5}$$

where a is the Van der Waals radius of the bead and η is the viscosity of water. The timestep used for Langevin dynamics was based on the characteristic time, τ, that is defined as

$$\tau = \sqrt{\frac{m}{k_s}} \tag{S6}$$

where m is the maximum bead mass. The timestep was adjusted to match the diffusion of a bead attached to a spring. Using this technique, the timestep was determined to be 43.4 fs or τ/20.

In order to model the dynamics of the coarse-grained model, the Langevin dynamics equation was solved using a generalized Verlet algorithm (1)

$$\dot{x}^{n+1/2} = \dot{x}^n + m^{-1}\frac{\Delta t}{2}\left[-\nabla E(x^n) - \gamma M\dot{x}^n + R^n\right] \tag{S7}$$

$$x^{n+1} = x^n + \Delta t\dot{x}^{n+1/2} \tag{S8}$$

$$\dot{x}^{n+1} = \dot{x}^{n+1/2} + m^{-1}\frac{\Delta t}{2}\left[-\nabla E(x^{n+1}) - \gamma M\dot{x}^{n+1} + R^{n+1}\right] \tag{S9}$$

where n is the timestep. The position is calculated from the half velocity, and then the position and half velocity are both used to calculate the full velocity.

2. ENM Reference State

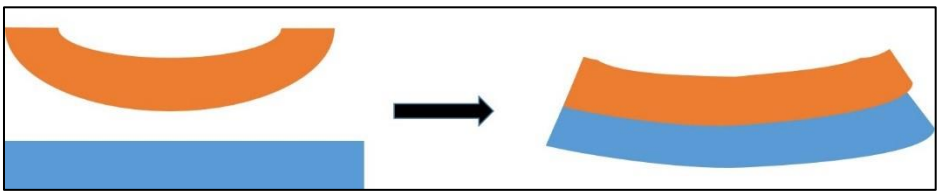

FIGURE S1 A model showing two beams. The reference or zero energy state for both beams is when they are separated from each other. When the beams form a bundle, mutual interactions deform them into some shape with associated stored energy that will be released when the beams are separated.

For each of the helices there exists a relaxed, natural, or reference state, and we maintain that the relaxed state of the springs that comprise the elastic network model should be defined in this reference state. This idea is illustrated in the figure above. Say we have two helices (orange and blue) with two different reference states (bent and straight). When the two helices come into contact with each other, they will both deform to form an equilibrium structure. If we assume the energy of the system to be 0 on the left, some energy is required to bend both helices to form the combined structure on the right. In our model we use our references states, like those on the left,

to help us calculate the energy stored in the bundle that can be released as the bundle is pulled apart.

The existence of such a reference state is not contingent upon its viability as a stable state for an actual isolated helix. Although Syb by itself is largely unstructured, we can still define the Syb helix by itself, i.e., removed from the other SNARE helices. It is a notional state used merely to obtain the frozen or stored elastic energy in the SNARE bundle. That is, all that is required is that the helical forms be stable as a bundle and that we have a systematic procedure by which to define springs on a relaxed state, again, regardless of whether the relaxed state actually exists.

We recognize that in many sources in the literature it is noted that Syb is largely unstructured when not in the presence of the SNARE bundle. We conducted 40 ns all-atom simulation of the individual SNARE helices, starting with a configuration extracted from the crystal structure. We found that this timescale was more than sufficient to allow all of the helices to straighten into relatively straight rod-like conformations. It was also short enough that each rod retained its helical structure. Because of this separation of time scales – time to relax an individual helix << time required for it to lose it structure – we were able to define the natural or reference state of each helix on which to construct the elastic spring network.

3. Determining the cut-off distance and spring constant in the elastic network model for SNARES

Coordinates from the straightened out helical structures were extracted from the individual AA simulations, and the connectivity and natural length of the ENM springs for each helix were determined based on these structures. If the cutoff distance is too small, the proteins will denature. If it is too large, simulation speed will be compromised with no significant improvement in representation. In order to find an optimal value, this distance was adjusted and a histogram was created for each helix to show the total number of springs that were connected to each bead. The minimum criterion for the number of springs was that each bead should be connected by a spring to all of its nearest neighbors. It was concluded that a cutoff distance of a minimum of 10 Å yielded at least 4 springs per bead, which satisfied this criteria. After further investigation, it was determined that R_c was required to be at least 20 Å in order to maintain the helical structure of each helix during AA simulations. The histogram for the final value of R_c, 20 Å, for the helix Syb is shown in Fig. S2. The histograms for the other three helices are similar.

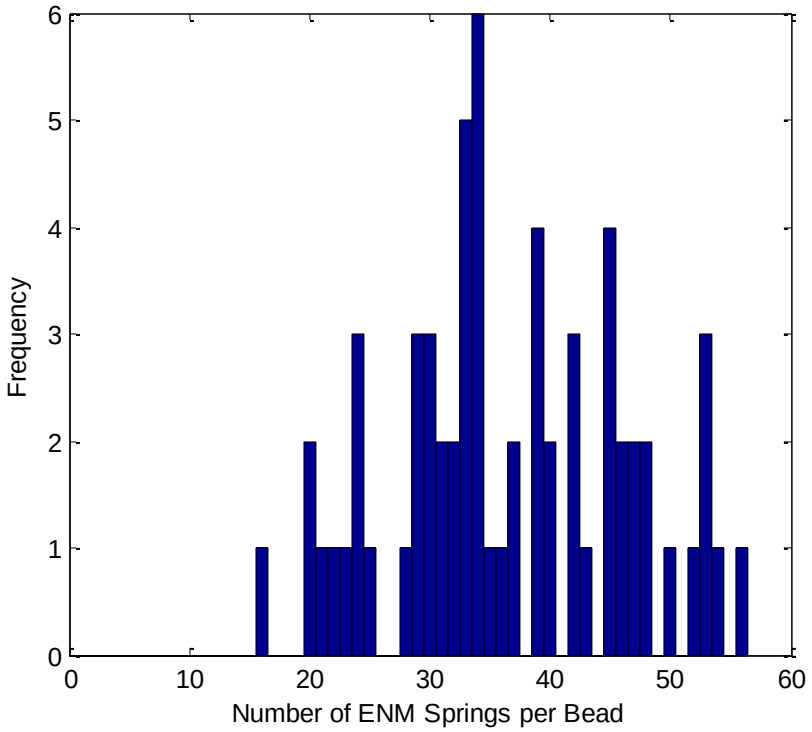

FIGURE S2 A histogram for the number of ENM springs per bead is shown for Syb with a value of 20 Å for R_c.

The values of k_s for the ENM were chosen by matching the spectrum of fluctuations of the AA simulations and the CG model. For the analysis of individual AA helix simulations, the positions of the alpha carbons were extracted every 10 ps. For each alpha carbon a time series of distance from average location was calculated. The fast Fourier transform (FFT) was then evaluated for each bead's time series. The average was taken over all beads yielding a single spectrum per helix. In order to make this comparison of the fluctuations, CG simulations were conducted for the 4 individual helices using Langevin dynamics at 300 K for a range of values of k_s. The time length of simulations required was determined by conducting a normal modes analysis (NMA) on the CG model of the crystal structure, 1N7S, for all helices individually using different values of k_s. AA simulations were run for 2 ns, which is considerably longer than the characteristic time given as the inverse of the lowest natural frequency. The results for Syb are shown in Table S1.

TABLE S1 The lowest natural frequencies and characteristic times for Syb determined are shown below for different values of k_s

k_s (N/m)	Lowest Natural Frequency Squared $(1/ns)^2$	Time (ns)
0.0963	4.53	4.70E-01
0.1926	9.05	3.32E-01
0.2889	1.36	2.71E-01
0.3853	1.81	2.35E-01
0.4816	2.26	2.10E-01

For Syb, as was seen for all helices, the characteristic times are significantly less than 1 ns. As a result the AA simulations were analyzed for the first 2 ns of the trajectories, and the CG test simulations were conducted for 2 ns and analyzed with data collected every 2 ps. In order to best match the fluctuations, the root mean squared deviation (RMSD) between the AA and CG spectra was found for each run. An example of the comparison of both spectra is shown in Fig. S3 for Syb with k_s value of 0.0963 N/m. The RMSD for all helices for all values of k_s are shown in Table S2 with the minimum RMSD values shaded in grey.

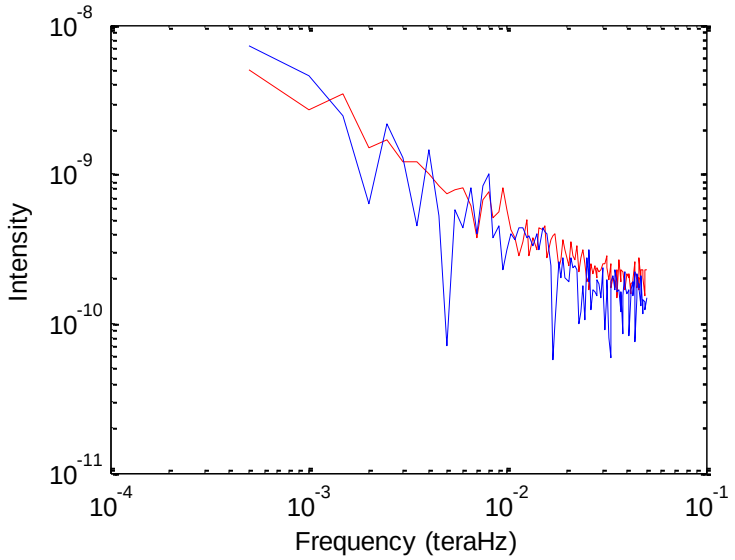

FIGURE S3 The spectra used to compare the fluctuations of the AA (*blue*) and CG (*red*) models are shown for Syb for 2 ns. Values of k_s as 0.0963 N/m and R_c of 20 Å were used for the CG model. An RMSD of 4.7E-10 was found.

TABLE S2 The RMSD values between the AA and CG fluctuation spectra are shown below for all helices for a range of values of k_s. The minimum RMSD values are shaded in grey.

k_s (N/m)	Syb RMSD	Syx RMSD	SN1 RMSD	SN2 RMSD
0.00009	9.6450e-09	1.0532e-08	1.2658e-08	9.5905e-09
0.0009	4.9432e-09	5.5075e-09	6.7327e-09	4.6640e-09
0.0096	1.4341e-09	1.1056e-09	1.5941e-09	1.7538e-09
0.0481	7.4334e-10	1.4651e-09	8.5729e-10	1.6778e-09
0.0963	4.7077e-10	4.3346e-10	1.3671e-09	2.3080e-09
0.1444	7.2271e-10	9.9229e-10	1.5680e-09	1.1604e-09
0.1926	1.4341e-09	1.1064e-09	1.5941e-09	1.7539e-09
0.2889	1.2019e-09	1.5654e-09	2.7382e-09	3.0644e-09
0.3853	1.7372e-09	2.0310e-09	3.2207e-09	3.3413e-09
0.4816	2.4969e-09	2.8429e-09	3.2951e-09	3.5652e-09

Based on the data in Table S2, a value of 0.0963 N/m was chosen for k_s for all four helices. For Syb and Syx, this corresponds to the value of k_s with the smallest RMSD. For SN1 and SN2 however, the minimum RMSD occurs either a little above or below k_s of 0.0963 N/m. Because the RMSD is still very small for these two helices with that value of k_s, it was chosen to use a consistent value of k_s for all helices.

4. Calibration of λ and displacement orientation

As described in the SNARE CG model portion in the methods section, the value of λ was adjusted in order to match the peak force reported by Gao et al. (3) of 14 – 19 pN. We conducted a series of displacement control simulations at 0K for a set of λ values ranging from 0.30 to 0.72. Displacement was applied in steps and the system allowed to relax. Relaxation to equilibrium was monitored by tracking the forces acting on the C-terminal beads of Syb and Syx as shown in Fig. S4. Each force spike corresponds to a displacement being applied to the C-terminal bead of Syb. After 10^5 timesteps, both forces relax to nearly the same value, which is taken as the equilibrium force for that displacement, and the next displacement step is then applied.

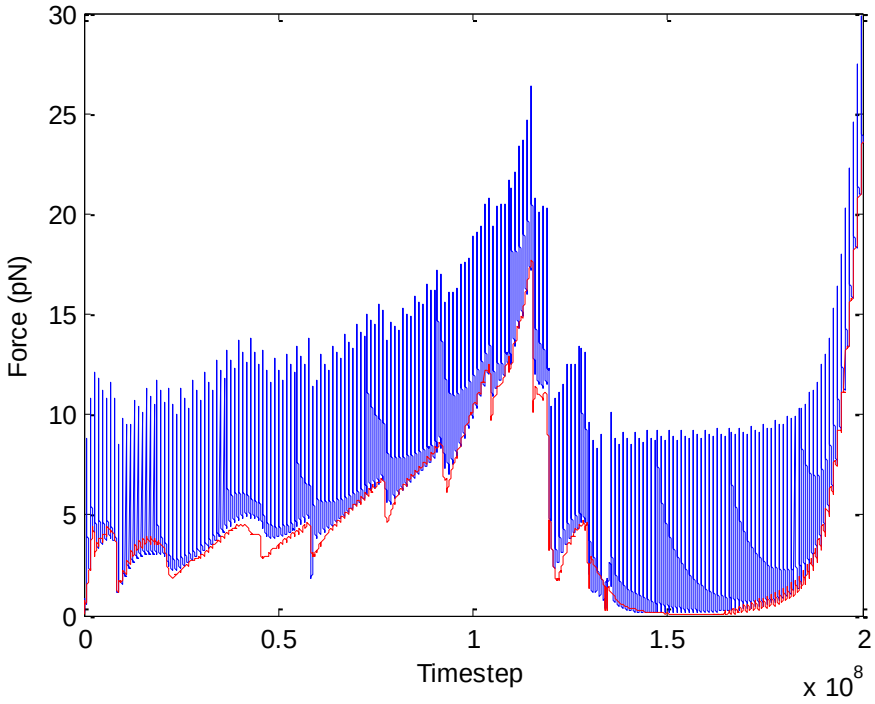

FIGURE S4 The force as a function of timestep is shown for a displacement control run with λ set to 0.30. The forces on the C-terminal beads of Syb (*blue*) and Syx (*red*) are shown. Each spike in the Syb force corresponds to application of a new displacement step. A total displacement of 20 nm is shown.

The resulting force displacement curves for a few of these runs for varying λ are shown in Fig. S5.

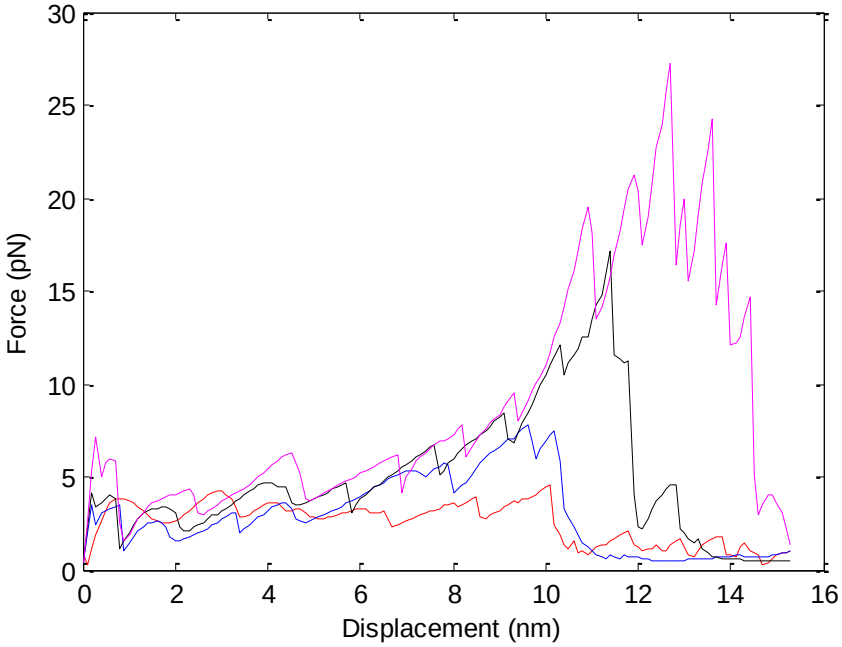

FIGURE S5 Force displacement curves are shown for displacement control simulations done using λ values of 0.16 (*red*), 0.24 (*blue*), 0.30 (*black*), and 0.40 (*magenta*).

It was clear that as λ was increased, the peak force increased as well. By choosing its value to be 0.3, we attained a peak force of 17.2 pN that lies in the experimentally measured range.

5. SNARE Force Displacement Instabilities and Their Effect on Energy

There are several mechanical instabilities in the force-separation curve of the SNARE, for example at 7.5 nm in Fig. 3 *C*. These usually correspond to "breaking" of one of the layers. When the system jumps from one stable point to the next, it does not follow the equilibrium force-separation relationship between these two points; instead, it lies above it. When we integrate the force-separation curve to obtain energies, we consequently compute a slightly larger magnitude (more negative) than it should be. This does not affect any of the predictions about stable equilibria.

6. Continuum Governing Equations and Their Solution

The axisymmetric deformation of the vesicle-membrane system can be reduced to the solution of a set of ordinary differential equations. The undeformed configuration of the vesicle is a sphere of radius R with arc-length in a cross-section denoted by S whereas, the plasma membrane occupies the interior of a circle of radius L R. We introduce the notation ϕ to denote the angle made by the tangent to a point on the cross-section of the deformed membrane in the (r,z) plane with the z axis (see Fig. S5 *A*). Briefly, the equations describing the deformation involve the shear force Q, the angle ϕ, the mean curvature H, the deformed arc length ξ, the deformed coordinates of a generic material point (r,z) which has an arc length coordinate S in the undeformed configuration. To expedite the analysis, we introduce the following normalized variables:

$$\bar{S}=\frac{S}{R},\quad \bar{r}=\frac{r}{R},\quad \bar{z}=\frac{z}{R},\quad \bar{H}=RH,\quad \bar{\xi}=\frac{\xi}{R},$$
$$\bar{Q}=\frac{QR^2}{c},\ \bar{d}=\frac{dR^2}{c}, \tag{S10}$$
$$\bar{p}_0=\frac{p_0R^3}{c},\ \bar{F}_e=\frac{F_eR^3}{c},\ \bar{F}_n=\frac{F_nR^3}{c},\ \bar{F}_t=\frac{F_tR^3}{c},$$

where,

p_0 is the osmotic pressure of the vesicle,

d is an integration constant resulting from integrating the tangential force equilibrium equation (see supplementary information for details),

F_e is the electrostatic force per unit area of the membrane and is always along z direction,

F_t is the tangential component of the concentrated load at the material point S_0 in the deformed membrane,

F_n is the normal component of the concentrated load at the material point S_0 deformed membrane.

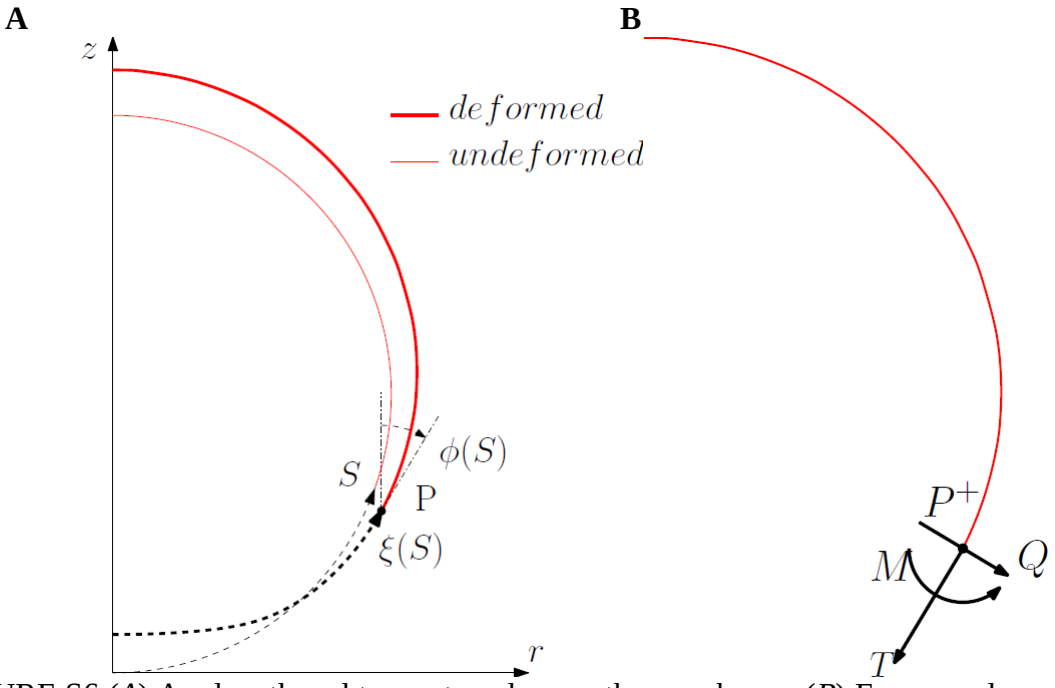

FIGURE S6 (*A*) Arc length and tangent angle over the membrane, (*B*) Forces and moment along the cut in the membrane.

As shown above non-dimensionalization of all the length scales is done by the radius of the undeformed vesicle, R. As c has units of energy, we use it to non-dimensionalize force per unit length quantities i.e. in-plane tension, T and out of plane shear, Q by c/R^2. Also force per unit area quantities, p_0, F_e, F_t and F_n are made dimensionless by c/R^3.

Also, in both the loading conditions it has been assumed that the F_t for vesicle is always zero. There are six ordinary differential equations governing the deformation of the vesicle membrane, they are:

$$\dot{\bar{Q}} = -\frac{\bar{Q}}{\bar{r}}\dot{\bar{\xi}}\sin\phi - 2\bar{H}\dot{\bar{\xi}}\left[\bar{d} + \bar{H}^2 + \left(2\bar{H} + \frac{\cos\phi}{\bar{r}}\right)\frac{\cos\phi}{\bar{r}}\right] + \dot{\bar{\xi}}\,\bar{p},$$

$$\dot{\phi} = \dot{\bar{\xi}}\left(2\bar{H} + \frac{\cos\phi}{\bar{r}}\right),$$

$$\dot{\bar{H}} = \dot{\bar{\xi}}\bar{Q},$$

$$\dot{\bar{r}} = \dot{\bar{\xi}}\sin\phi,$$

$$\dot{\bar{z}} = \dot{\bar{\xi}}\cos\phi,$$

$$\dot{\bar{d}} = \left(\bar{F}_e\cos\phi + \bar{F}_t\right)\dot{\bar{\xi}} \qquad \text{(S11a-S11f)}$$

where, the dot denotes differentiation with respect to the normalized undeformed arc length $\bar{S}$, and

$$\dot{\bar{\xi}} \equiv \frac{\sin\bar{S}}{\bar{r}} \quad . \qquad \text{(S11g)}$$

The normalized normal force acting on the deformed membrane surface, $\bar{p}$ in Eq. S11a is related to the osmotic pressure of the vesicle, $\bar{p}_0$, the electrostatic force per unit area, $\bar{F}_e$ and the normal component of the concentrated load applied at $\bar{S} = \bar{S}_0$, $\bar{F}_n$ by,

$$\bar{p} = \bar{p}_0 + \bar{F}_e\sin\phi + \bar{F}_n\delta\left(\bar{S} - \bar{S}_0\right) \qquad \text{(S11h)}$$

where, $\delta(\bar{S} - \bar{S}_0)$ is the Dirac delta function.

These differential equations are supplemented with the boundary conditions:

$$\phi(\bar{S} = 0) = \frac{\pi}{2},$$

$$\bar{Q}(\bar{S} = 0) = 0,$$

$$\bar{r}(\bar{S} = 0) = 0,$$

$$\phi(\bar{S} = \pi) = -\frac{\pi}{2},$$

$$\bar{Q}(\bar{S} = \pi) = 0,$$

$$\bar{r}(\bar{S} = \pi) = 0, \qquad \text{(S12a-S12f)}$$

The boundary conditions defined above essentially represent the symmetry in the vesicle geometry. About the symmetry axis, the curve has zero slope and out of plane shear $\bar{Q}$ is zero, at both $\bar{S} = 0$ and π. Also, for the continuity of the geometry, we impose $\bar{r} = 0$ at both $\bar{S} = 0$ and π.

The notation for positive shear force and tension is described in Fig. S6. Finally, the expression for the in-plane tension in both the vesicle and plasma membrane is given by,

$$\bar{T} = \frac{TR^2}{c} = \frac{R^2}{c}\left(-d - cH^2 - cH\frac{cos\phi}{r}\right). \qquad (S13)$$

The governing equations for the deformation of the plasma membrane is very similar, except that Eq. *S*11g must be replaced by,

$$\dot{\bar{\xi}} = \frac{\bar{S}}{\bar{r}} \qquad (S14)$$

This change is due to the difference between the reference configurations. The boundary conditions are:

$$\begin{aligned}
&\phi(\bar{S}=0) = \frac{\pi}{2},\\
&\bar{Q}(\bar{S}=0) = 0,\\
&\bar{r}(\bar{S}=0) = 0,\\
&\phi\left(\bar{S}=\frac{L}{R}\right) = \frac{\pi}{2},\\
&\bar{z}\left(\bar{S}=\frac{L}{R}\right) = 0,\\
&\bar{T}\left(\bar{S}=\frac{L}{R}\right) = \left[-\bar{d} - \bar{H}^2 - \bar{H}\frac{cos\phi}{\bar{r}}\right]_{\bar{S}=\frac{L}{R}} = \bar{T}_0 \equiv \frac{T_0R^2}{c}
\end{aligned} \qquad (S15a\text{-}S15f)$$

The boundary conditions at $\bar{S} = 0$ is due to axisymmetry. Eq. *S*15f states that the tension in the plasma membrane approaches the pretension at the boundary. This boundary condition allows the neuron membrane to deflect. Had we replaced this boundary condition with a clamped condition, the deflection everywhere would be zero because of area incompressibility.
The coupled ODE's in Eqs. *S*11 - *S*15 with the boundary conditions are solved using the MATLAB® bvp4c solver. The input parameters for the solver are the osmotic pressure p_0 across the vesicle membrane which remains fixed throughout the deformation, SNARE-machinery force parameters (S_0 and magnitude F), electrostatic force and pretension (T_0) in the plasma membrane.

7. Example problem of continuum model

Here we show an example of the results of the calculation of vesicle-membrane interaction. In this example, the location of force application is fixed at $\bar{S}_0 = \frac{\pi}{6}$ on both the vesicle and neuron base, as shown in Fig. S7. This location of load application corresponds to the number of SNAREs of 21. Parameters used in the continuum model are shown in Table S3.

TABLE S3 Parameters used for the continuum model of the vesicle and plasma membrane

Parameter	**Value**	**Comment**
Permittivity of vaccum, ε_0	8.85 x 10^{-12} Fm^{-1}	

Dielectric constant of water, ε	80	dimensionless
Ion concentration inside neuron, c_0	200 mM (4)	(1-1) electrolyte
Debye length, l_D	0.67nm	$l_D = \sqrt{\frac{\varepsilon\varepsilon_o k_B T}{2q^2 z^2 c_o}}$
Synaptic vesicle radius, R	20nm (5)	
Surface charge of vesicle and inside of plasma membrane, σ_1 and σ_2	-0.025 Cm^{-2}, -0.025 Cm^{-2} (5–7)	
Surface potential of vesicle and inside of plasma membrane, φ_1 and φ_2	-25 mV, -25 mV	
Bending rigidity of lipid bilayer, c	~20 k_BT (8)	8.28 x 10^{-20} J

The strength of the line force is varied in the range of $5-20$ in dimensionless terms, which is equivalent to a net force between $66-266\ pN$. Fig. S7 shows the deformed shapes of the membranes for four different values of $\bar{F}$. The inset on the right shows the calculated relationship between applied force and separation between load application points. The force decreases rapidly with increasing separation, reflecting the steep decay of the electrostatic repulsion.

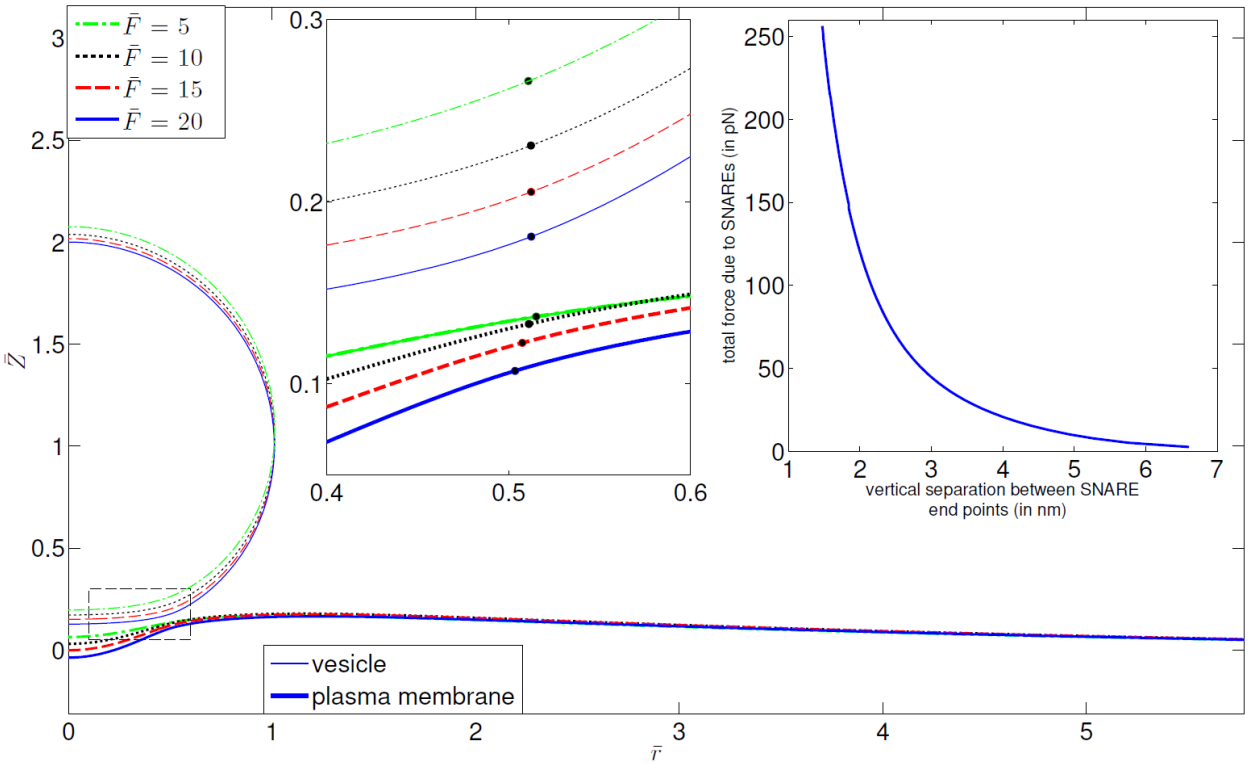

FIGURE S7 Deformed geometry for different force magnitudes. The thick lines represent the neuron base and the thin lines represent the vesicle. The inset on the left shows the zoomed in section of the load application point (*shown as* •) and the inset on the right shows the vertical separation between the two ends of SNARE-machinery versus the net SNARE force. The

parameters are for the analysis are: load application point, $\bar{S}_0 = \pi/6$, pretension in plasma membrane, $\bar{T}_0 = 1$ and vesicle pressure. $\bar{p}_0 = 1$.

8. SNARE Force Separation Curve Shift

To compare the attractive force imposed by the SNARE bundle to the repulsive force on the vesicle, we need a consistent definition of separation. The distance connecting the final residue beads (Syb89 and Syx256) is shorter than the distance between the outside membrane surfaces due to the presence of other parts of the SNARE. To address this issue, we created a static coarse grained structure of a 20 nm vesicle and plasma membrane with a partially opened SNARE at its equilibrium configuration as shown in the figure below. We found that distance between the outer surface of the membranes is actually about ~1nm further apart than the distance between Syb89 and Syx256. We have therefore added this distance when comparing the attractive force on the SNARE to the repulsive force on the vesicle. Adding the initial separation between Syb89 and Syx256, the minimum distance allowed between the membranes at the point of force application is about 2nm. Another related effect is that inter-SNARE-bundle repulsion can increase the minimum lateral separation. We have considered two additional cases where we take lateral SNARE bundle width to be 2 and 4 nm (an additional Debye screening length increase in radius in the latter case). The larger lateral spacing makes the effect of number of SNAREs significantly stronger but the minimum separation and the number of SNAREs needed to achieve it does not change much.

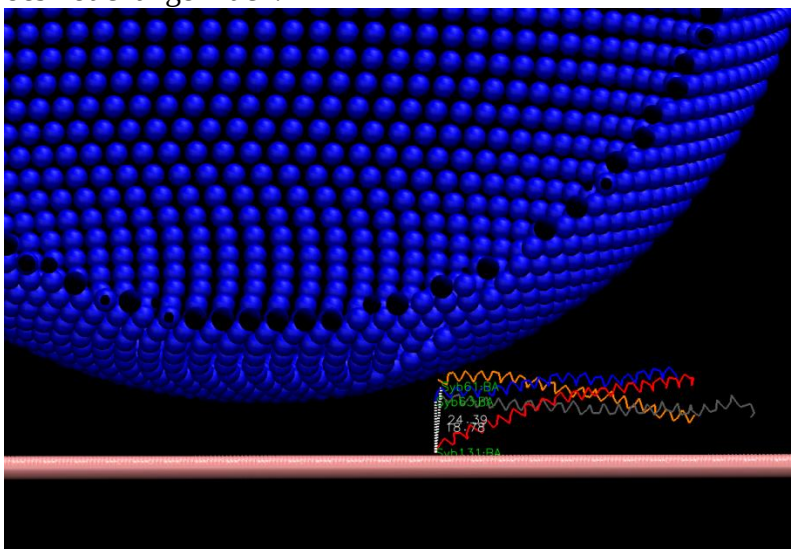

Figure S8. Drawing of a vesicle near a plane along with a model for the SNARE bundle.

9. Choice of SNARE Model

The CG simulation model was built using the SNARE X-ray crystal structure 1N7S that includes Syb (27-89), Syx (189-256), SN1 (5-83), and SN2 (139-204). We recognize that this structure only includes part of the Syb linker domain (85-95) and none of the linker domain of Syx (256-266). However, we believe that our choice of placing the membrane outer surface at residues 89 and 256 is correct. Our choice is based on the following papers (9, 10) that show Syb insertion in the membrane starts at Trp 89. Specifically, they show that 89-94 is unstructured but is

inserted in the membrane. Similarly, the following paper shows that for Syx, residues after 261 are in the lipid bilayer. Specifically, 261-266 are unstructured but inside the lipid bilayer (11). The following study (12) also concludes that the linker domains (256-266) and (85-95) are buried in the top layer of the membrane. Because the reference distance from the hydration repulsion is the outer surface of the membrane, to be consistent we believe that it is quite appropriate to define SNARE displacement from 88 for Syb to 256 for Syx, within some uncertainty of a just a few residues.

Whether or not the linker domains have unraveled is debatable. It was shown in Gao et al's optical tweezer experiment that the Syb linker domain unravels at 10-13 pN. Because the equilibrium SNARE end-end distances of interest in this work are <~ 3nm), our maximum force only reaches (<5pN) and neglecting helix unraveling in our model is justifiable. Nevertheless, in order to check the robustness of our solution against unraveling, we did melt two helical turns of Syb (including up to residue 91). The principal effect is that the minimum equilibrium separation increases from 2 nm to 2.5 nm for both hydration and electrostatic repulsion with a constant charge.

10. Robustness of Model Results

To judge the sensitivity of our main conclusions on the various assumptions we have made, we carried out a number of other simulations. Our main conclusion is that the principal results of our model are quite robust with respect to uncertainty in the assumptions made.

10.1. Electrostatics: We explored how electrostatics would affect the vesicle to plasma membrane repulsion. Fig. S9 shows results for the case where hydration repulsion is replaced by electrostatics using a fixed surface charge of -0.025 C/m^2 on the vesicle and the membrane. Evidently, with these parameters the electrostatic repulsion is weaker than the hydration repulsion. For one SNARE the end separation is ~2.4nm, which is smaller than the 3 nm seen for the hydration repulsion case (Fig. 4 *B*). However, when more than 1 SNARE is added to the system, the equilibrium SNARE end separation is constant at ~2 nm for 2-13 SNAREs, that is, it would be completely zippered shut.

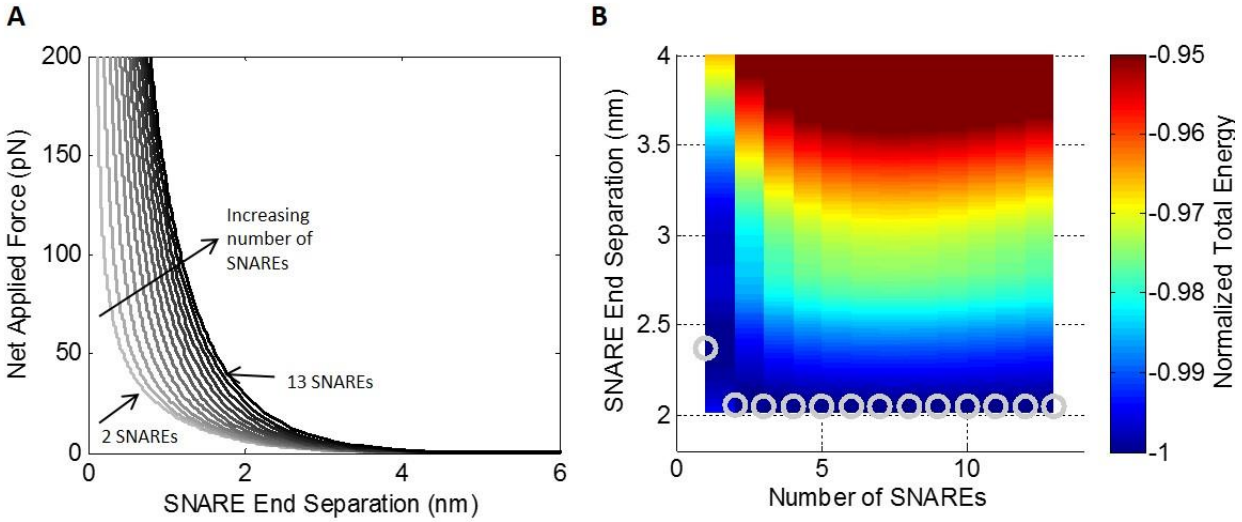

FIGURE S9 (*A*) The force in the membrane/vesicle system is shown as a function of SNARE end separation for a vesicle radius of 20nm with electrostatic repulsion with a fixed surface charge. (*B*) The corresponding contour plot of total energy as a function of SNARE end

separation distance and the number of SNAREs. Gray circles correspond to global energy minima representing the equilibrium SNARE end separation for a given number of SNAREs.

10.2. Larger vesicles:Although our primary interest is in the smaller synaptic vesicles, the model can also be applied to study larger vesicles. Fig. S10 shows results for the case of a 100 nm vesicle.

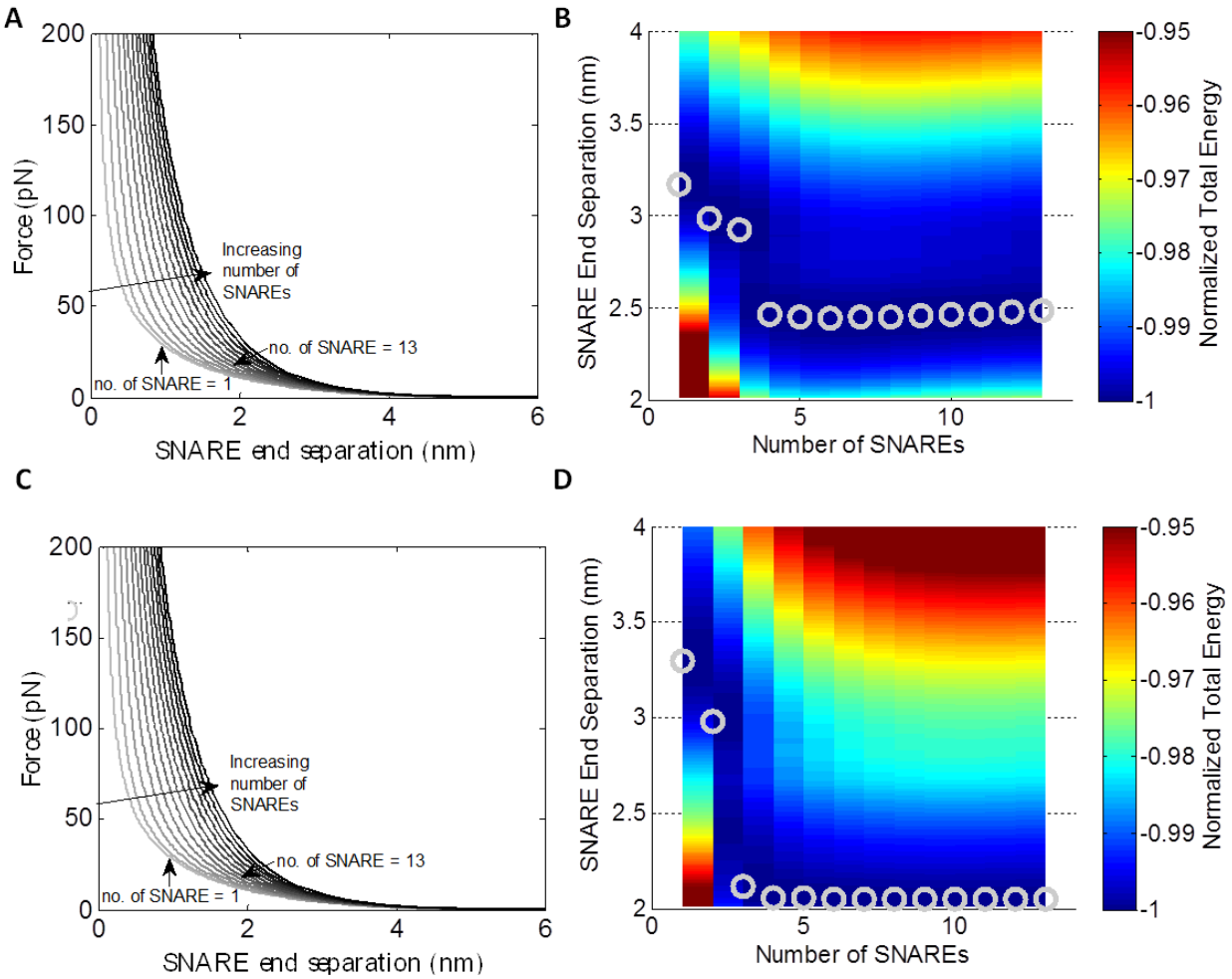

FIGURE S10 The force in the membrane/vesicle system is shown as a function of SNARE end separation for a vesicle radius of 100nm with (*A*) hydration repulsion and (*C*) electrostatic repulsion with a fixed surface charge. Contour plots of total energy as a function of SNARE end separation distance and the number of SNAREs are shown for a vesicle radius of 100nm with (*B*) hydration repulsion and (*D*) electrostatic repulsion with a fixed surface charge. Gray circles correspond to global energy minima representing the equilibrium SNARE end separation for a given number of SNAREs.

For the hydration repulsion case the minima are significantly larger than those found for the 20nm case shown in Fig. 4 *B*. For four or more SNAREs the equilibrium separation is ~2.5nm which is different from the 20nm case where the separation is ~2nm and the SNARE bundle can be nearly fully zippered. For the case of electrostatic repulsion, for larger number of SNAREs the repulsion is still insufficient to open the SNARE except when there is are three or fewer SNAREs.

10.3. Fixed Potential: We also carried out computations assuming a fixed potential of -25 mV on the vesicle and on the membrane as opposed to the fixed surface charge case that was assumed in the majority of the paper. The resulting force separation curves for the 20nm and 100nm vesicle cases are very similar to the case of fixed charge. This is not unexpected because the electrostatic force for fixed charge versus fixed potential cases becomes nearly the same for separations greater than the Debye screening length.

10.4. Unraveling of Syb: Several other modifications were made to the cases shown in Fig. 4. There is some question about whether part of the syb helix unravels. We have argued that the forces are small enough that the helical structure should be preserved. However, to test the effect on our prediction of potential unraveling, we allowed 2 helical turns to unravel and be represented by elasticity of a worm-like chain coil. Because the Syb helix touches the membrane at residue 91 and the CG model only contains up to residue 89, an extra 2 residues were added to the unraveled portion of Syb. The force displacement curve for the melted portions of Syb were modeled using a worm like chain model following Gao et al.(3) The force extension relationship was calculated using the Marko-Siggia formula

$$F = \frac{k_B T}{P_{melt}}\left[\frac{1}{4\left(1-\frac{x_{melt}}{L_{melt}}\right)^2}+\frac{x_{melt}}{L_{melt}}-\frac{1}{4}\right] \qquad (S16)$$

where P_{melt} is the persistence length of the melted segment (0.6 nm) and x_{melt} is the end to end distance of the melted segment. L_{melt}, the maximum end to end distance of the melted segment, was calculated assuming a 0.365 nm contour length per residue (3) which totaled to 1.3 nm due to ~2 helical turns being melted. The master force displacement curve was slightly adjusted by deleting the portions of the curve that corresponded to the 7 residues that are now accounted for using the WLC model. The SNARE end separation, x_{SNARE}, was defined by

$$x_{SNARE}(F) = x_{melt}(F) + x_{bundle}(F) + BW \qquad (S17)$$

where x_{melt} is the end to end distance of the melted portion of Syb, x_{bundle} is described using the manipulated master force curve described in this section, and BW is the width of the SNARE bundle or the distance between the Syb and Syx C-termini when no external force is being applied. The corresponding results are shown is shown in Fig. S11 *A* for a 20nm vesicle with hydration repulsion and Fig. S12 *A* for a 20nm vesicle with electrostatic repulsion and a fixed surface charge.

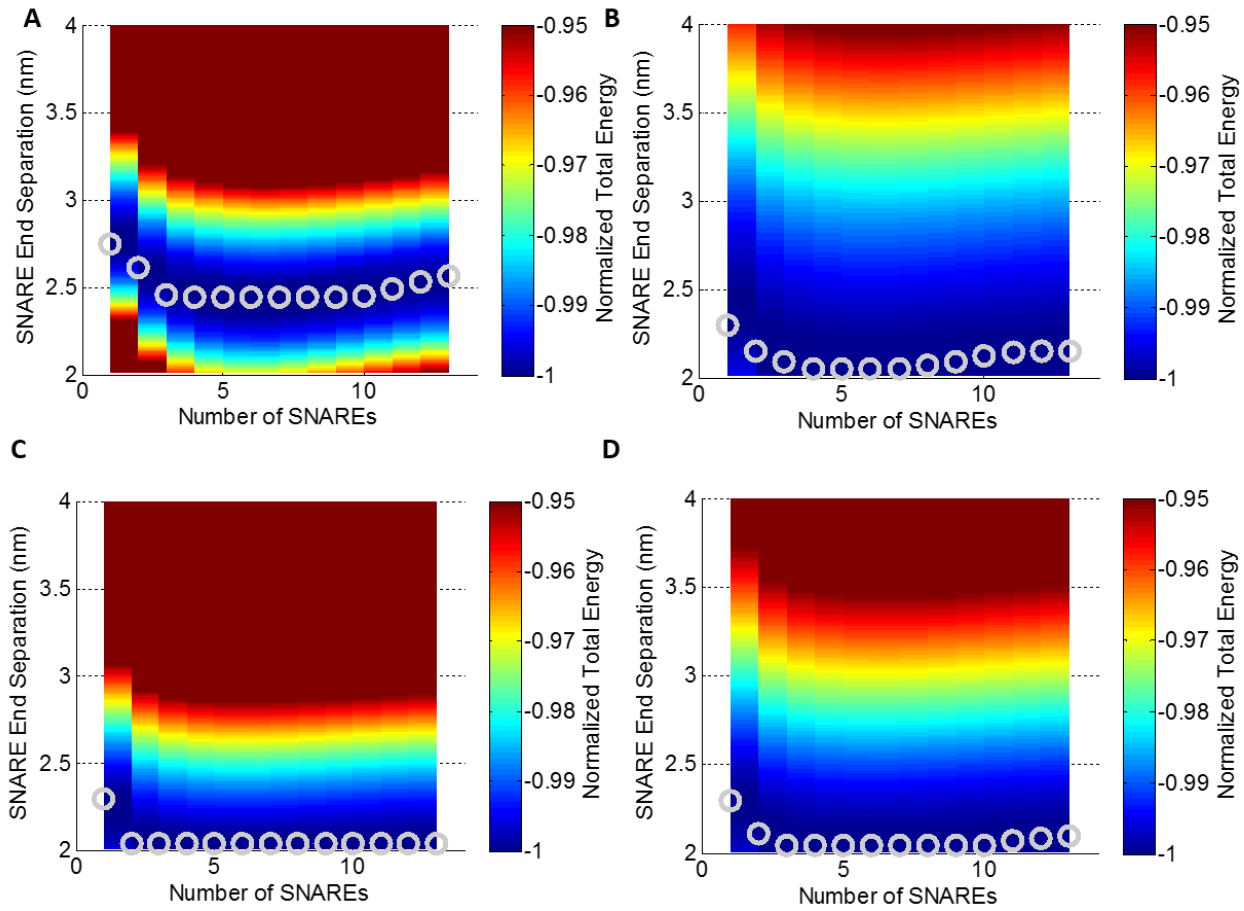

FIGURE S11 For a 20nm vesicle with hydration repulsion, contour plots of normalized total energy as a function of SNARE end separation distance and the number of SNAREs are shown. Gray circles correspond to energy minima representing the equilibrium SNARE end separation for a given number of SNAREs. Several cases are shown: (*A*) 2 helical turns unraveled, (*B*) Syx frozen, (*C*) SNAP25 frozen, and (*D*) Syx and SNAP25 frozen.

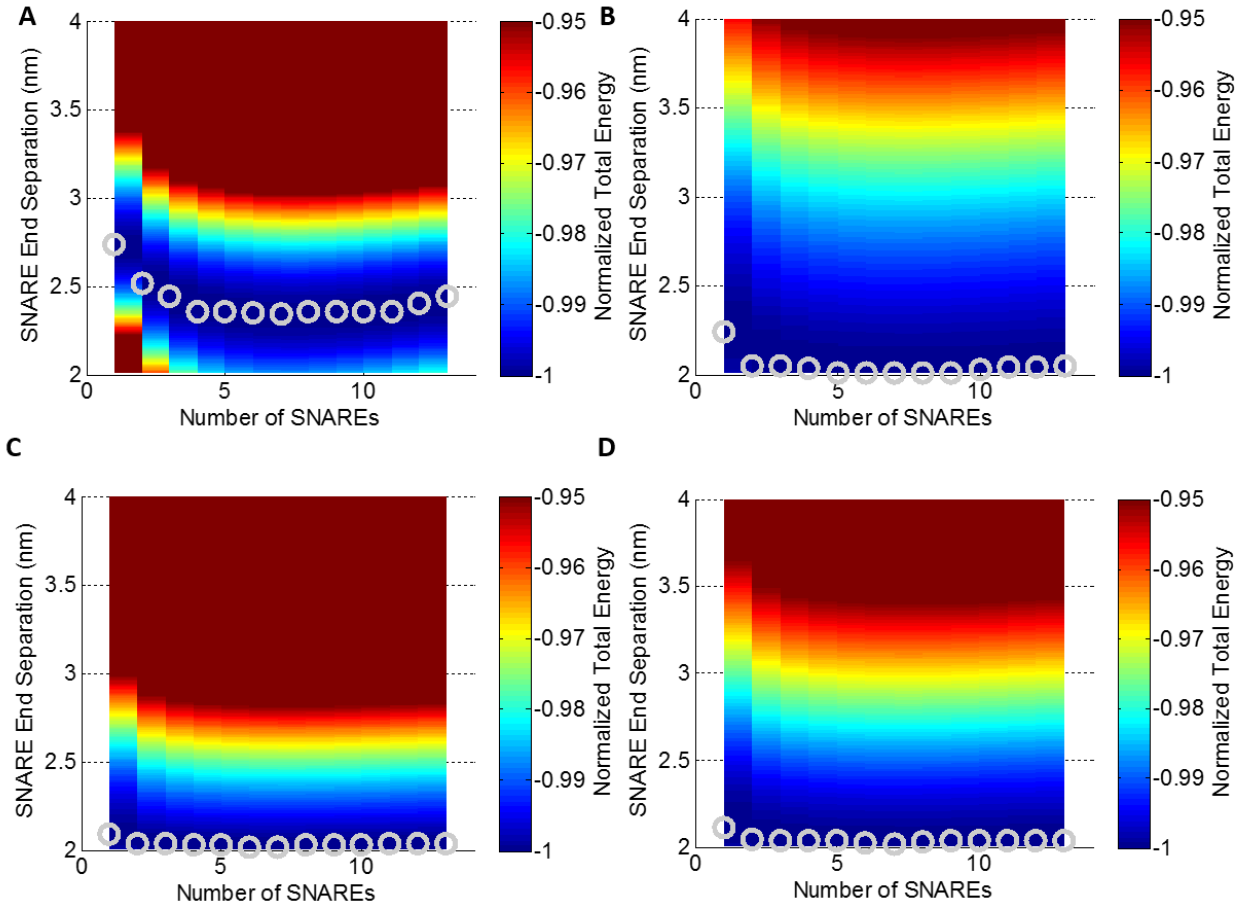

FIGURE S12 For a 20nm vesicle with electrostatic repulsion assuming a fixed surface charge, contour plots of normalized total energy as a function of SNARE end separation distance and the number of SNAREs are shown. Gray circles correspond to energy minima representing the equilibrium SNARE end separation for a given number of SNAREs. Several cases are shown: (*A*) 2 helical turns unraveled, (*B*) Syx frozen, (*C*) SNAP25 frozen, and (*D*) Syx and SNAP25 frozen.

In both cases, the results differ from those seen in Fig. 4 when unraveling was not permitted. For the case of hydration repulsion, the minimum separation is somewhat larger (~2.4 nm) than that shown in Fig. 4 *B* (~2.1 nm). There is a similar difference for the case of electrostatic repulsion.

10.5. Freezing SNAP25 or Syx: In our simulations we allowed SNAP25 helices to be free to adjust their orientation. This mimics the optical tweezers experiment used to calibrate our model. However, the situation *in vivo* is likely different with SNAP25 and/or Syx constrained against motion. In order to see the effects of the positioning of SNAP25 in relation to the SNARE bundle we studied three variations: freezing Syx, freezing SNAP25, and freezing both Syx and SNAP25. When Syx was frozen, SNAP25 still remained associated with Syb. Anytime that SNAP25 was frozen at all, it remained associated with Syx. The energy calculations were repeated for the hydration repulsion case (Fig. S11) and the electrostatic repulsion case with fixed surface charge (Fig. S12). The freezing of helices in all of these cases has little effect on the minimum distance and number of SNAREs. The principal difference occurs for the one-SNARE case where the equilibrium distance reduces significantly.

10.6. High Osmotic Pressure and Low Pretension Limit

Figs. 2 and S7 show cases of low osmotic pressure and plasma membrane tension where the plasma membrane bulges near the axis of symmetry because the attractive forces draw the two membranes to each other at their point of application but near the axis of symmetry only repulsion acts. Experiments suggest that prior to vesicle to membrane fusion, the vesicle retains its spherical shape while the plasma membrane surface conforms when the two are in contact (13, 14). The continuum model was recalculated using high osmotic pressure in the vesicle and low pretension in the plasma membrane with constant potential. The resulting structures are shown for 10 and 15 SNAREs in Fig. S16.

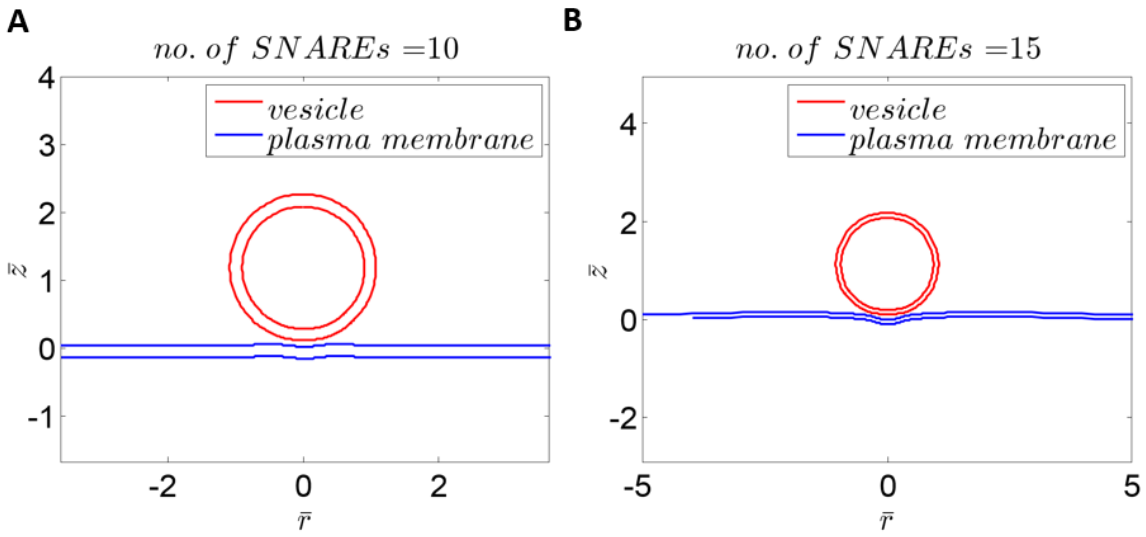

FIGURE S13 For a 20nm vesicle with high osmotic pressure and low pretension in the plasma membrane with constant potential the vesicle and plasma membrane structures are shown including their bilayer thickness for (*A*) 10 SNAREs and (*B*) 15 SNAREs.

Under the conditions of high osmotic pressure and low pretension when 10 SNAREs are present there is little bulging of the plasma membrane and the vesicle remains spherical when the vesicle and plasma membrane are brought together. The separation is relatively constant which is consistent with the Malsam et al.(13) and Hernandez et al. (14). As the number of SNAREs is increased to 15, there is some bulging in the plasma membrane at the axis of symmetry. The vesicle has retained its spherical shape while the plasma membrane bends to conform to it.

The energy surface for this case is shown in Fig. S14. We note that there is little difference between these and those of Fig. 4 *B*. This suggests that our model is robust with respect to this uncertainty. (In particular, the value of vesicle osmotic pressure is difficult to estimate.)

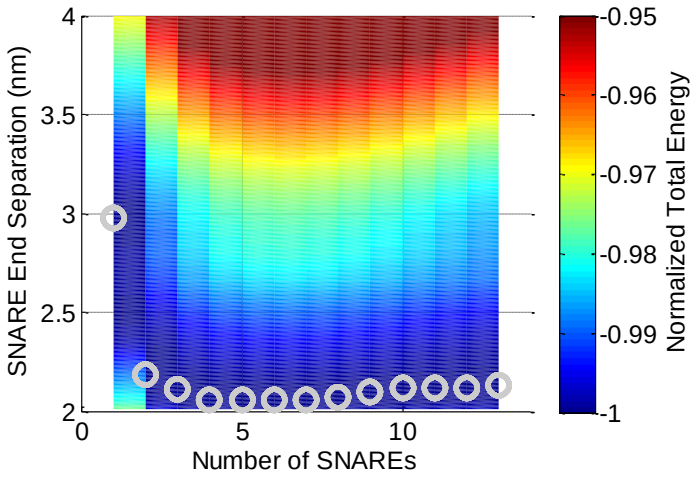

FIGURE S14 Contour of normalized total energy as a function of SNARE end separation and number of SNAREs for a 20nm vesicle with high osmotic pressure and low pretension in the plasma membrane, and with constant potential on the vesicle and plasma membrane. White circles correspond to energy minima representing the equilibrium SNARE end separation for a given number of SNAREs.

10.7. <u>High Vesicle Pressure, High Membrane Tension Vesicle-Membrane Model</u>

In order to display the effects of the deformation considered in the continuum model, a more simplified analytical model of the Vesicle-Membrane system based on Bykhovskaia et al.(15) was calculated. The parameters used in the analytical model were consistent with those used in the continuum model as described in Section 2.3. Consider the case in which vesicle pressure P_o and the membrane tension T are sufficiently large such that neither the vesicle nor the membrane deform as they approach each other. In this case Bykhovskaia et al.(15) have shown that the force between the vesicle and membrane is given by

$$F = \frac{2\pi R\varepsilon\varepsilon_0}{l_D}\left(\frac{2\varphi_1\varphi_2}{\sinh\left(\frac{a}{l_D}\right)} - (\varphi_1^2+\varphi_2^2)\left(\coth\left(\frac{a}{l_D}\right)-1\right)\right) \tag{S18}$$

for fixed surface potential and

$$F = \frac{\pi R l_D}{\varepsilon\varepsilon_0}\left(\frac{2\sigma_1\sigma_2}{\sinh\left(\frac{a}{l_D}\right)} + (\sigma_1^2+\sigma_2^2)\left(\coth\left(\frac{a}{l_D}\right)-1\right)\right) \tag{S19}$$

for fixed charge. The force separation curves are shown for the vesicle-plasma membrane for several cases using this model in Figs. S15 and S16.

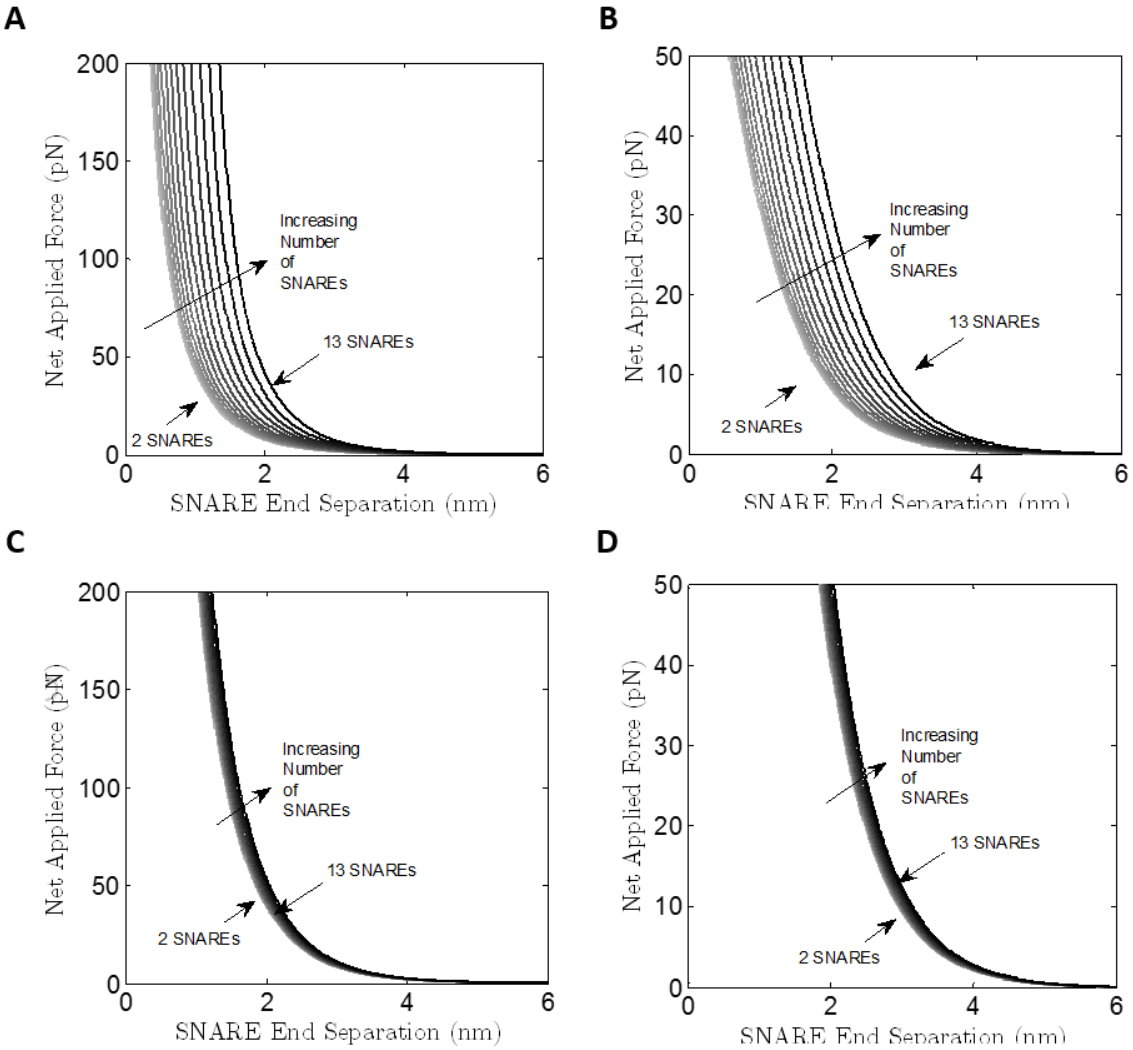

FIGURE S15 For the high vesicle pressure high membrane tension limiting case, the net applied force in the membrane/vesicle system is shown as a function of SNARE end separation for a vesicle with a (*A*) 20nm radius with fixed charge, (*B*) 20nm radius with fixed surface potential, (*C*) 100nm radius with fixed charge, and (*D*) 100nm radius with fixed surface potential.

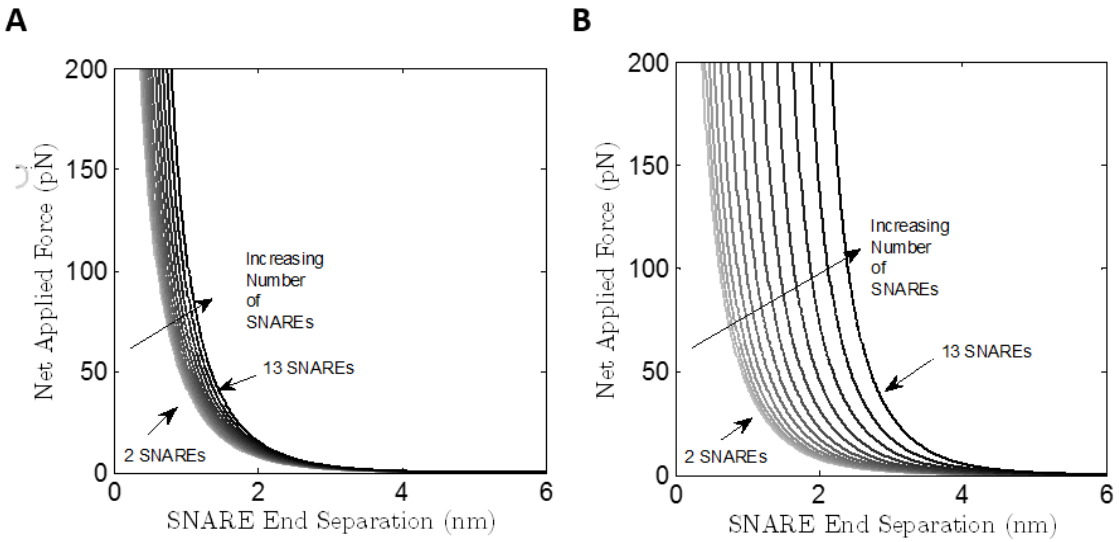

FIGURE S16 For the high vesicle pressure high membrane tension limiting case, the net applied force in the membrane/vesicle system is shown as a function of SNARE end separation for a radius for a vesicle with a 20nm radius with fixed charge when (*A*) the SNARE bundle diameter is 2nm and (*B*) the SNARE bundle diameter is 2nm.

10.8. Effect of Lateral Bundle Width: Figure S17 shows results of a test of the sensitivity of the solution to the location of the SNAREs when the lateral size of the SNARE bundle was varied from 2nm in Fig. S17 *A* to 4nm in Fig. S17 *B* (the base case used is 3nm, Fig. 4 *B*). Increasing the lateral width of the SNARE bundle seems to have a significant effect on the solution. There is a minimum separation at 4 SNAREs. With the addition of more than 5 SNAREs the equilibrium separation again begins to increase all the way up to ~3nm with 13 SNAREs.

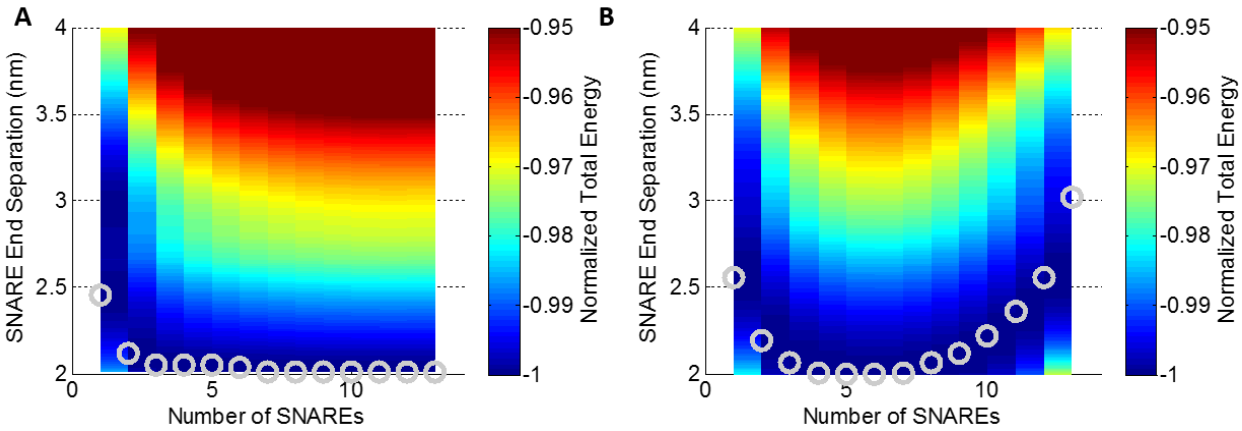

FIGURE S17 For the high pressure high tension limiting case, contour plots of normalized total energy as a function of SNARE end separation distance and the number of SNAREs are shown. Gray circles correspond to energy minima representing the equilibrium SNARE end separation for a given number of SNAREs. Several cases are shown for the vesicle with a radius of 20nm and fixed charge. The size of the SNARE bundle was varied to (*A*) 2nm and (*B*) 4nm.

11. SUPPORTING REFERENCES

1. Schlick, T. 2002. Molecular modeling and simulation: an interdisciplinary guide. New York: Springer.

2. Kubo, R. 2002. The fluctuation-dissipation theorem. Reports Prog. Phys. 29: 255–284.

3. Gao, Y., S. Zorman, G. Gundersen, Z. Xi, L. Ma, G. Sirinakis, J.E. Rothman, and Y. Zhang. 2012. Single reconstituted neuronal SNARE complexes zipper in three distinct stages. Science. 337: 1340–3.

4. Bruce Alberts Julian Lewis Keith Roberts, and Peter Walter, Alexander Johnson, M.R. 2002. Molecular Biology of the Cell. 4th ed. New York: Garland Science.

5. Ohsawa, K., H. Ohshima, and S. Ohki. 1981. Surface potential and surface charge density of the cerebral-cortex synaptic vesicle and stability of vesicle suspension. Biochim Biophys Acta. 648: 206–214.

6. Marra, J. 1986. Direct measurement of the interaction between phosphatidylglycerol bilayers in aqueous electrolyte solutions. Biophys. J. 50: 815–825.

7. Pekker, M., and M.N. Shneider. 2014. The surface charge of a cell lipid membrane. arXiv Prepr. arXiv. : 1401–1407.

8. Deserno, M. Fluid lipid membranes – a primer. 2007. http://www.cmu.edu/biolphys/deserno/pdf/membrane_theory.pdf

9. Kweon, D.H., C.S. Kim, and Y.K. Shin. 2002. The membrane-dipped neuronal SNARE complex: A site-directed spin labeling electron paramagnetic resonance study. Biochemistry. 41: 9264–9268.

10. Kweon, D.-H., C.S. Kim, and Y.-K. Shin. 2003. Regulation of neuronal SNARE assembly by the membrane. Nat. Struct. Biol. 10: 440–447.

11. Kim, C.S., D.H. Kweon, and Y.K. Shin. 2002. Membrane topologies of neuronal SNARE folding intermediates. Biochemistry. 41: 10928–10933.

12. Stein, A., G. Weber, M.C. Wahl, and R. Jahn. 2009. Helical extension of the neuronal SNARE complex into the membrane. Nature. 460: 525–528.

13. Malsam, J., D. Parisotto, T.A.M. Bharat, A. Scheutzow, J.M. Krause, J.A.G. Briggs, and T.H. Söllner. 2012. Complexin arrests a pool of docked vesicles for fast Ca2+-dependent release. EMBO J. 31: 3270–3281.

14. Hernandez, J.M., A. Stein, E. Behrmann, D. Riedel, A. Cypionka, Z. Farsi, P.J. Walla, S. Raunser, and R. Jahn. 2012. Membrane Fusion Intermediates via Directional and Full Assembly of the SNARE Complex. Science (80-.). 336: 1581–1584.

15. Bykhovskaia, M., A. Jagota, A. Gonzalez, A. Vasin, and J.T. Littleton. 2013. Interaction of the complexin accessory helix with the C-terminus of the SNARE complex: molecular-dynamics model of the fusion clamp. Biophys J. 105: 679–690.